Heavy Ion Beam Diagnostic of MHD Instabilities in the Compact Helical System

Seishu Lee

A Thesis Submitted to the
Department of Fusion Science
School of Mathematical and Physical Science
The Graduate University for Advanced Studies
in Candidacy for the Degree
of Doctor of Philosophy

Major Subject: Physics

National Institute for Fusion Science
November 1996

ABSTRACT

The heliotron/torsatron devices are regarded as an attractive candidate for a fusion reactor because of their steady state operation without inductive plasma currents. In these devices major disruptions induced by current driven instabilities can be avoided. However, they are susceptible to pressure driven instabilities such as interchange modes and ballooning modes, which limit high-β operation. Recent theoretical study suggests that such instabilities also contribute to enhance anomalous transport and deteriorate the confinement. In the Compact Helical System (CHS), magnetic fluctuations have been studied by the use of poloidal and toroidal arrays of magnetic probes. It has been found that the fluctuation modes depend on magnetic configuration, beta value, direction of beam induced current during NBI heating (which can change the magnetic shear), and so on. Among these fluctuations, periodic, burst type m/n=2/1 (m: poloidal mode number, n: toroidal mode number) modes observed in a low-β, NBI (co-injected) plasma have shown the strongest activity.

The oscillations appear periodically, typically every 4 milliseconds, and their frequency generally decreases from 40kHz to 15kHz during a growing phase. The mode is considered to be an interchange instability. However, the mode, propagating initially in the ion diamagnetic drift direction, reverses the direction (to the electron diamagnetic drift direction) in the decaying phase. In addition, the role of the magnetic fluctuations on confinement has not been clarified yet. Local and direct measurements of the internal structure is necessary for further investigation.

We have applied the heavy ion beam probe (HIBP) for the first time to measure MHD instabilities in helical system. The HIBP is a unique and powerful technique which can directly measure the electric potential and its fluctuations in high temperature plasmas. It has been successfully applied to tokamaks, mirrors and bumpy tori in which toroidal field component is dominant on the beam path and the beam trajectories are basically two dimensional in the same poloidal plane. First application of HIBP to a helical device was done in the ATF torsatron, preliminary data has been reported also for MHD studies. HIBP measurements in helical devices are not so simple as in tokamak because of its three dimensional beam trajectories.

The CHS HIBP has two sets of beam deflectors to control the primary and secondary ion beams independently so that the injection angle of the secondary beam into the energy analyzer is kept constant during a radial scan. This method makes the observation area wider and improve accuracy in determining a plasma potential. Because an observation point is determined by the combination of four deflector voltages, it is inevitably sensitive to the accuracy of beam line alignment and fringing field of the deflectors. Experimental calibration is necessary to verify the accuracy of the total system. A movable detector and a gas ionization method have been applied to calibrate the beam trajectory and observation points. Sets of deflector voltages to observe locations along a radial scan line were experimentally obtained. The results agree well with the calculation. The movable detector is also used to optimize the focusing condition of the primary beam in the plasma region. Total calibration procedures with these methods have been successfully carried out.

In applying HIBP to measure the local space potential and its fluctuations during MHD activities, various non local effects (path integral effects along the beam trajectories) have to be examined. The effects of beam deflection and acceleration (or deceleration), which are caused by the fluctuating vector potential, on local potential fluctuation measurements are evaluated using the experimental data from HIBP and magnetic probes. By taking those effects into account, the radial structures of the m/n = 2/1 burst type MHD oscillation have been derived. The potential fluctuation has a strong peak around q = 2 surface in the growing phase and its amplitude is about 40 volts at maximum. The oscillation frequency decreases from 20 kHz to 10 kHz and the phase difference between the potential fluctuation and a Mirnov coil signal varies about 90 degree during the growing phase. The mode is propagating in the ion diamagnetic direction. At the end of the growing phase, the mode structure abruptly changes and the potential fluctuation is suppressed everywhere. The magnetic perturbation decays slowly at the constant frequency of 5 kHz (decaying phase). The maximum amplitude is larger than that in the growing phase. The propagation is in the electron diamagnetic direction and the mode appears to be fixed to the $E_r \times B_t$ plasma rotation (E_r: radial electric field, B_t: toroidal magnetic field) determined by the electrostatic potential. By considering those characteristics, the mode is considered to be an m/n = 2/1 interchange mode in the growing phase, although the propagation velocity and the growth rate are not fully explained. The mode structure in the decaying phase is completely different and is suggesting m = 2 island formation at the q = 2 rational surface.

In conclusion, the application of HIBP for the study of MHD instabilities in a helical plasma has been successfully carried out. Radial structure of the potential fluctuation associated with the m/n = 2/1 burst type interchange instability is experimentally clarified. The result demonstrates a new diagnostic approach to MHD fluctuation studies in helical plasmas.

Acknowledgement

The author wishes to express his sincere appreciation to Dr. Harukazu Iguchi for his useful and continuous discussions and advices on this work. The author would like to thank Prof. Yasuji Hamada for his many useful suggestions and encouragements all over his work. The author wishes to thank Dr. Akihide Fujisawa and Dr. Thomas P. Crowley of Rensselaer Polytechnic Institute for their useful supports and discussions on this study.

The author acknowledges the continuous encouragement by the Director-General of National Institute for Fusion Science, Prof. Atsuo Iiyoshi and Director of Department of Large Helical Device Project, Prof. Masami Fujiwara. The author also acknowledges the experimental support by Prof. Keisuke Matsuoka, Dr.Shoichi Okamura and all members of the CHS group and the NBI group. The author also wishes to thank Dr. Katsumi Ida and Mr. Shin Nishimura for providing the ion temperature data, and Dr. Takashi Minami and Dr. Kenji Tanaka for provided data from the Thomson scattering and HCN laser interferometer measurements, respectively. The author thanks to Mr. Mamoru Kojima and Mr. Chihiro Takahashi for their supports on HIBP and CHS data acquisition.

The author also would like to thank Prof. Kazuo Toi for his valuable suggestions and encouragement. Fruitful discussions with Drs. Noriyoshi Nakajima and Katsuji Ichiguchi are gratefully acknowledged. The author was partially supported by the fusion science association. Finally, the author would like to thank his parents, brothers, sister and Miss Akiko Fujiwara for their continuous encouragement and cooperation in his studies.

Contents

Chapter 1

Introduction

1.1 Overview

Magnetic plasma confinement is one of traditional ideas in the controlled thermonuclear fusion research. Various kind of configurations have been examined. The toroidal (doughnut-shaped) systems such as tokamaks or stellaraters are considered as to be the most promising. In tokamaks, plasmas are confined by the toroidal magnetic field B_T and the poloidal field B_θ produced by an inductive plasma current [1]. Plasma parameters comparable to break even have been obtained in large tokamaks such as JET, JT-60U and TFTR[2]. However, the plasma current is indispensable in tokamak operation, which can cause disruptive instabilities and limit steady state operation[3].

On the other hand, stellaraters (including heliotron/torsatrons) are regarded as an attractive candidate for a fusion reactor because of their steady state operation without inductive plasma current. In these devices current driven disruptive instabilities can be avoided[4]. However, they are susceptible to pressure driven instabilities such as interchange modes and ballooning modes, which limit high-β operation[5-8]. Recent theoretical study suggests that such instabilities also contribute to enhance the anomalous transport and deteriorate the confinement[9]. Studies of MHD instabilities are still major subjects in toroidal plasma confinement, for which advanced diagnostics are required.

In this thesis, a heavy ion beam probe (HIBP) is applied for the first time to measure magnetohydrodynamic (MHD) instabilities in a helical device. The HIBP is a unique and powerful technique which can directly measure the electrostatic potential and its fluctuations in high temperature plasmas. It has been successfully applied to tokamaks, mirrors and bumpy tori, where the beam trajectories are basically in a poloidal plane[10-17]. First application of HIBP to a helical device was done in the ATF torsatron, preliminary data has been reported on MHD fluctuations[18]. HIBP measurements in helical devices are not so simple as in tokamak because of its three dimensional beam trajectories[19]. The goals of this thesis are to examine the conditions for applying HIBP to measure MHD instabilities in a helical device and to discuss physical properties of such instabilities from HIBP data.

The next chapter will describe the basic principle of the heavy ion beam probe and hardwares of the CHS HIBP. Experimental calibrations are also included. The experimental results are presented in chapter 3. The data analyses, especially potential fluctuation measurements, are described in chapter 4. Physical interpretation of those experimental results and conclusion of this thesis are presented in chapter 5 and 6, respectively.

1.2 Diagnostics for MHD instabilities

Since the magnetohydrodynamic (MHD) instabilities are one of the serious issues to limit plasma performance and operation, many works to investigate MHD instabilities have been conducted[20]. Experimentally the magnetic probe (Mirnov coil) has been the most useful diagnostic method to measure magnetic fluctuations[21]. Numbers of probes are arranged poloidally and toroidally to determine poloidal and toroidal mode numbers. However, the coils are placed outside of the plasma, and detected signals are integrated value from all over the plasma area. Local internal structure of the fluctuations can not be derived.

MHD instabilities are also observed by Soft X-ray (SX) diode array[22]. The intensity of emission is a function of electron temperature and density along the sight line. Temporal and spatial structures of MHD behaviors are reconstructed from those data. The method has contributed to understand sawtooth oscillation, disruption and so on. However, a simple mode structure has to be assumed for the reconstruction. The ECE diagnostic is also used in a similar way as the SX array. The emission is in the wave length range from microwave to submillimeter wave range in this case, but the method of analysis is almost the same as that for the SX array.

Beam probe diagnostics have a capability of local and direct measurement of MHD instabilities. The Beam Emission Spectroscopy (BES) developed for plasma turbulence study, which generally utilizes a heating neutral beam, covers the long wavelength density fluctuations including MHD phenomena[22']. On the other hand, the heavy ion beam probe (HIBP) is a unique method to measure fluctuations of plasma potential as well as those of electron density. Application of HIBP to MHD fluctuations is expected to improve understanding of MHD behaviors in toroidal plasmas.

1.3 Compact Helical System (CHS)

CHS is a heliotron/torsatron device with a pole number of l=2, and a toroidal period number of m=8 (Fig. 1.1 and Table 1.1). The major and average minor radii are R=1.0m and a=0.20m, respectively. The rotational transform is 0.3 at the center and 1.0 at the periphery (Fig. 1.2).

Figure 1.1 shows a schematic view of the CHS device with heating and diagnostic systems. The electron temperature and density profiles are measured with Thomson scattering, and the line averaged electron density is determined by an HCN laser interferometer. The ion temperature profile is obtained by a charge exchange spectroscopy (CXS). To confirm the poloidal and toroidal fluctuation mode numbers of MHD instabilities, magnetic probe arrays have been used, which are arranged in 10 poloidal and 6 toroidal positions (Fig. 1.3). The radius and length of magnetic probes are 4 mm and 20 mm, respectively, and the number of turns is 260.

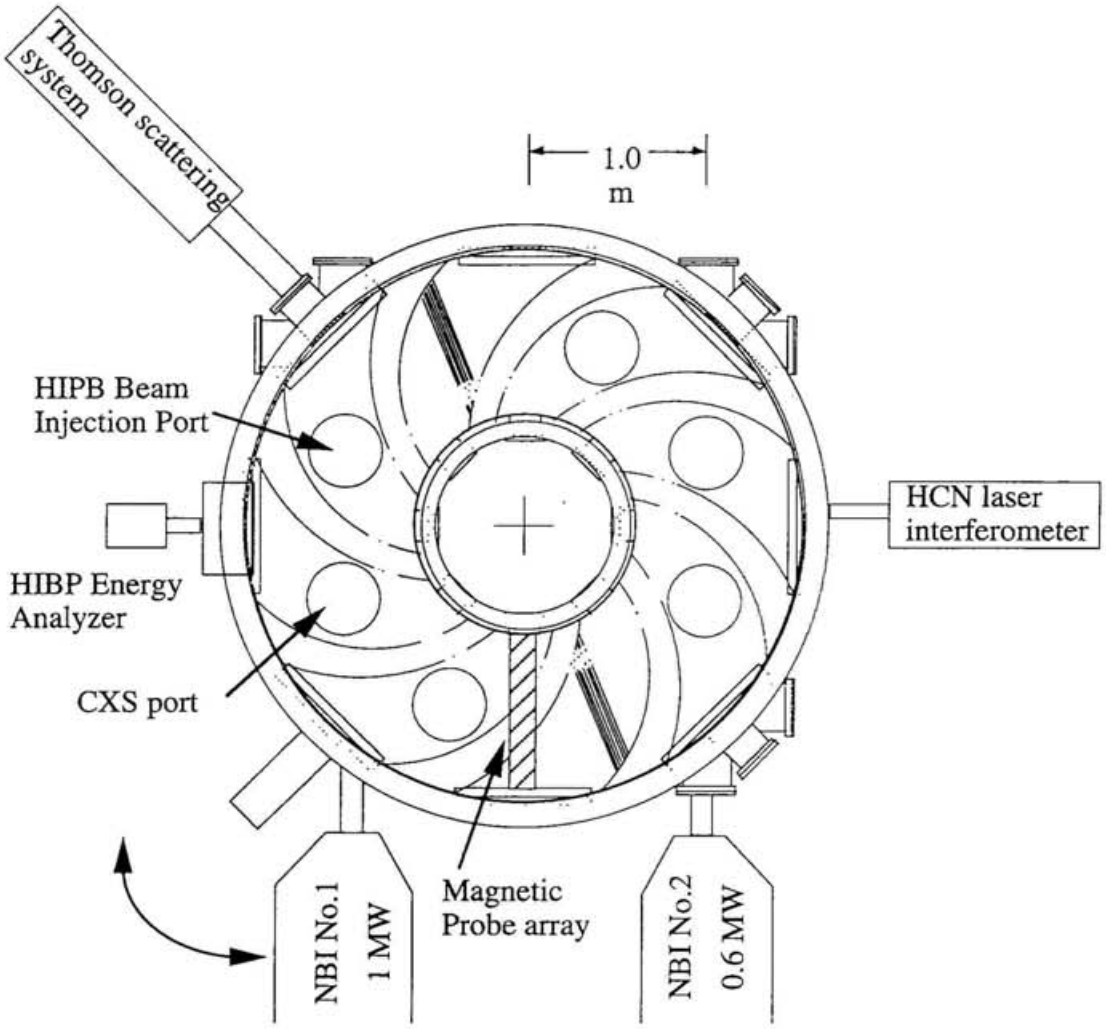

Figure 1.1 (a): A schematic view of the Compact Helical System (top view).

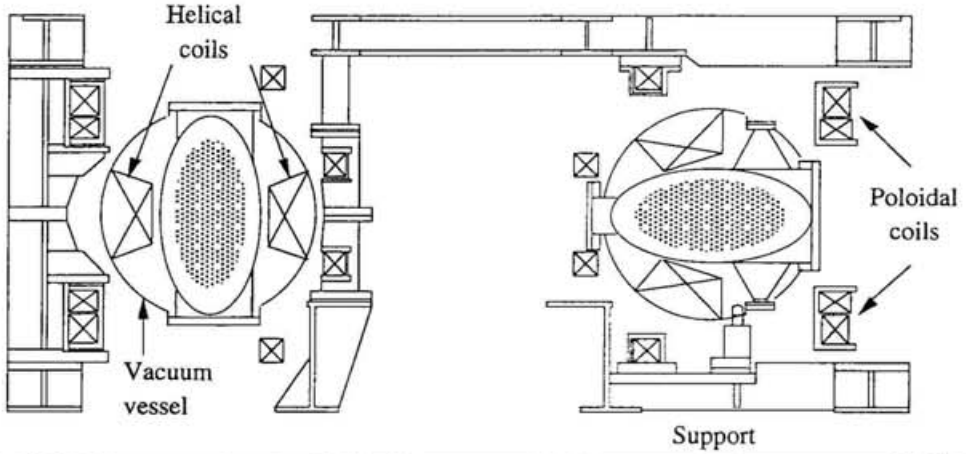

Figure 1.1 (b): A schematic view of the Compact Helical System (side view).

Parameter	Value
Major radius	1.0 m
Averaged minor radius	0.2 m
Aspect ratio	5
Polarity	2
Field period number	8
Pitch parameter	1.25
Pitch modulation	0.3
Field strength	2T
Rotational transform (center in vacuum)	0.3
(edge in vacuum)	0.8~1.0
Neutral beam power (No. 1)	1.1MW at 40kV
(No. 2)	0.7MW at 36kV
NBI pulse length	1 sec
ECH power	400/200 kW at 53GHz
	500 kW at 106GHz
ECH pulse length	100 ms
ICRF power	1.5MW
ICRF frequency	6~28MHz

Table 1.1: Specification of CHS

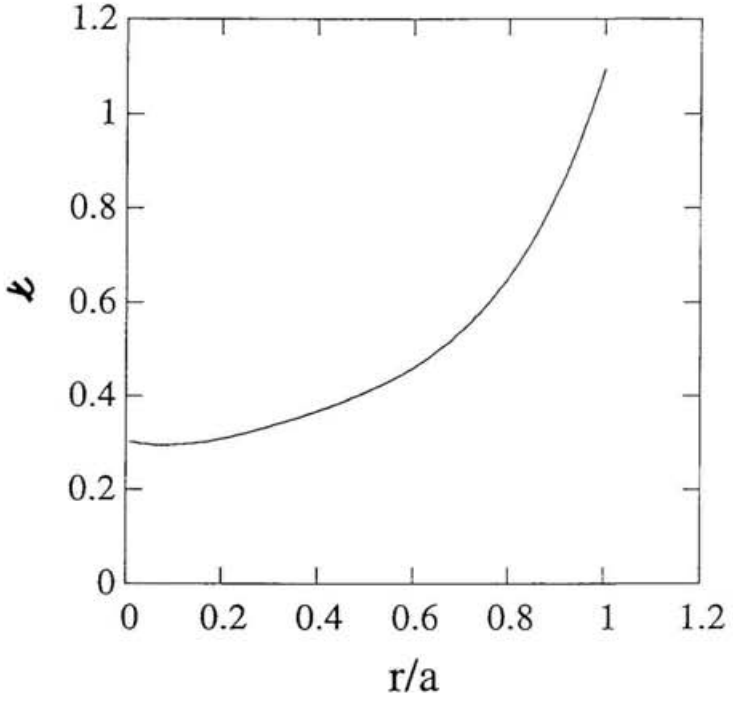

Figure 1.2: Rotational transform of CHS
(R_{axis} = 92.1cm, vacuum)

(a) Top view

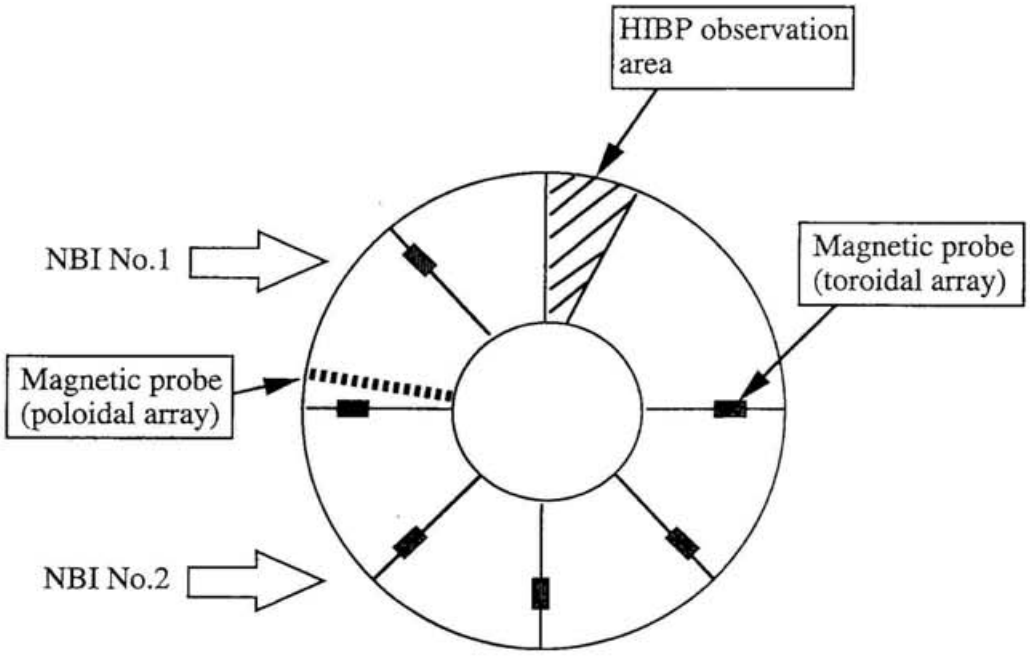

(b) Side view

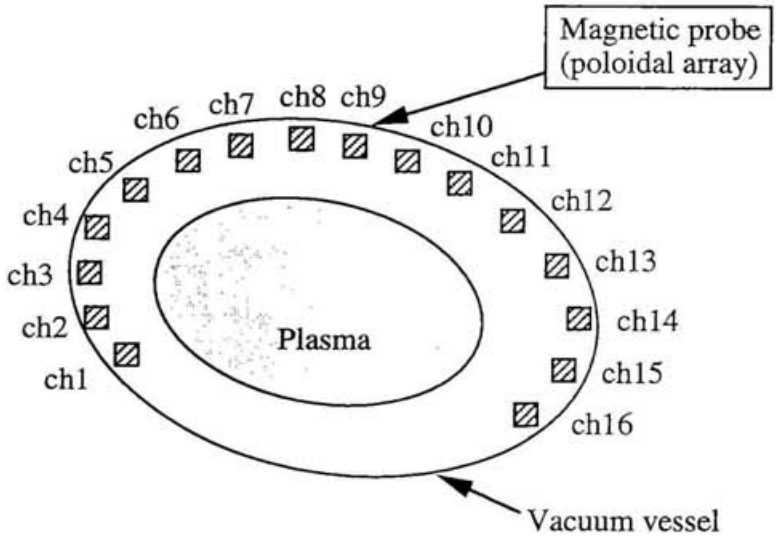

Figure 1.3: A schematic view of toroidal and poloidal magnetic probe array.

Chapter 2

The heavy ion beam probe diagnostic

2.1 Diagnostic Principles

The principle of the potential measurement by HIBP is illustrated in Fig. 2.1 [23]. A singly charged ion beam, called the primary beam, is injected into the magnetically confined plasma with the initial energy V_b. The electron impact with the primary beam ions produces doubly charged ions, called the secondary beam, when they pass through the plasma[24]. Among the secondary beams produced along the primary beam path, the beam which can reach the entrance slit of an energy analyzer can only be detected, for which the ionization position can be identified. As is shown in Fig. 2.2, the primary beam will have the energy of V_b-e ϕ at the ionization point (ϕ is the space potential at the ionization point), then the secondary beam ionized at this point will gain the energy of 2e ϕ at the exit point. Therefore the space potential is directly measured by comparing the energy change between the primary and secondary beams.

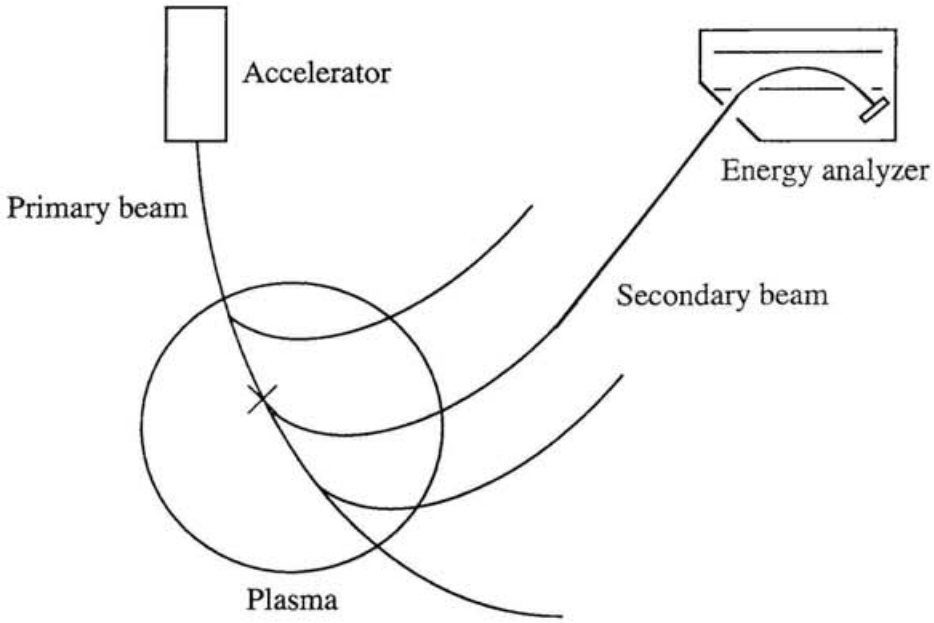

Figure 2.1: Schematic view of HIBP diagnostic principle

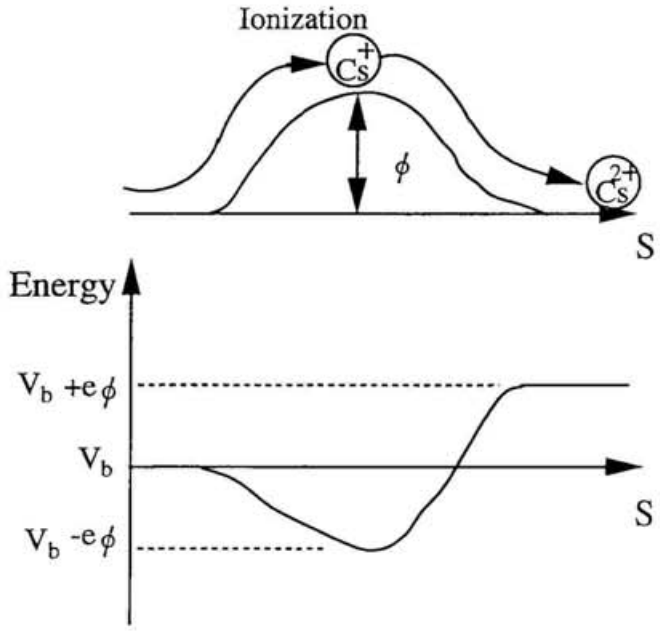

Figure 2.2: Principle of potential measurement

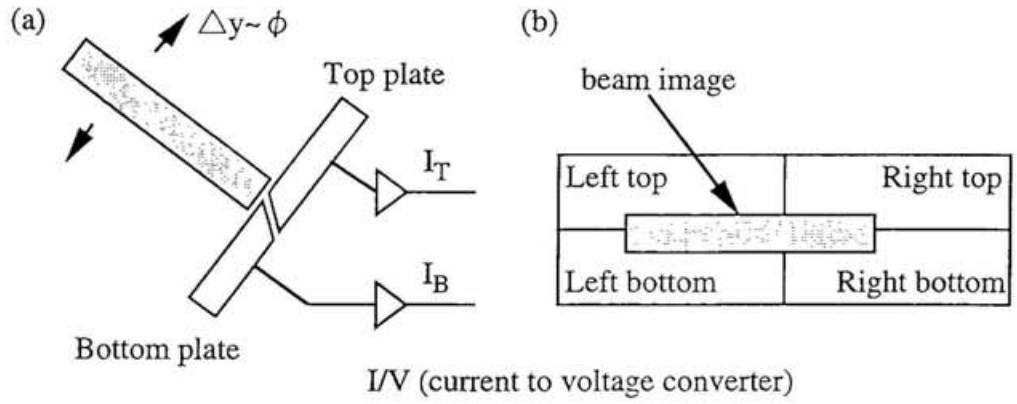

Figure 2.3: Schematic view of split plate detector (a) side view (b) front view

The energy of secondary beam is analyzed by the Proca and Green type parallel plate electrostatic energy analyzer with split plate detectors (SPD)[25,26]. An SPD set is composed of four detector plates, and the difference of the detected beam currents between top and bottom two plates normalized by their sum current ($(I_T-I_B)/I_{sum}$) is the measure of the energy change, namely, the plasma electric potential. The sum signal (I_{sum}) itself is proportional to the electron density and is the function of the electron temperature through ionization cross section at the observation point. The difference between left and right two plates normalized by the sum signal ($(I_L-I_R)/I_{sum}$) presents the beam displacement in the toroidal direction which is principally proportional to the poloidal magnetic field.

2.2 The CHS HIBP

2.2.1 Overview

A schematic view of the CHS HIBP is shown in Fig. 2.4. The primary and secondary beam lines are separated toroidally as shown in Fig. 2.5[19,27]. The ion source is a zeolite containing the cesium (or thallium) ions, which is made through chemical ion exchange reaction[28,29]. The ion source is heated up to several hundred degrees[30]. The ion beam is extracted from the Pierce type ion gun with a cylindrical eintzel lens (Fig. 2.6)[31,32]. Then the beam is accelerated up to 200 keV. Beamline position and beam profile are monitored by a rotating helical wire. A focus ladder detector (six parallel wires with 10 mm spacing) placed at the bottom port of CHS is used to adjust beam focusing. The secondary beam passing through a middle slit (70mm $\times$ 0~30mm) is introduced to the energy analyzer. The middle slits only used for the alignment check of the secondary beam line.

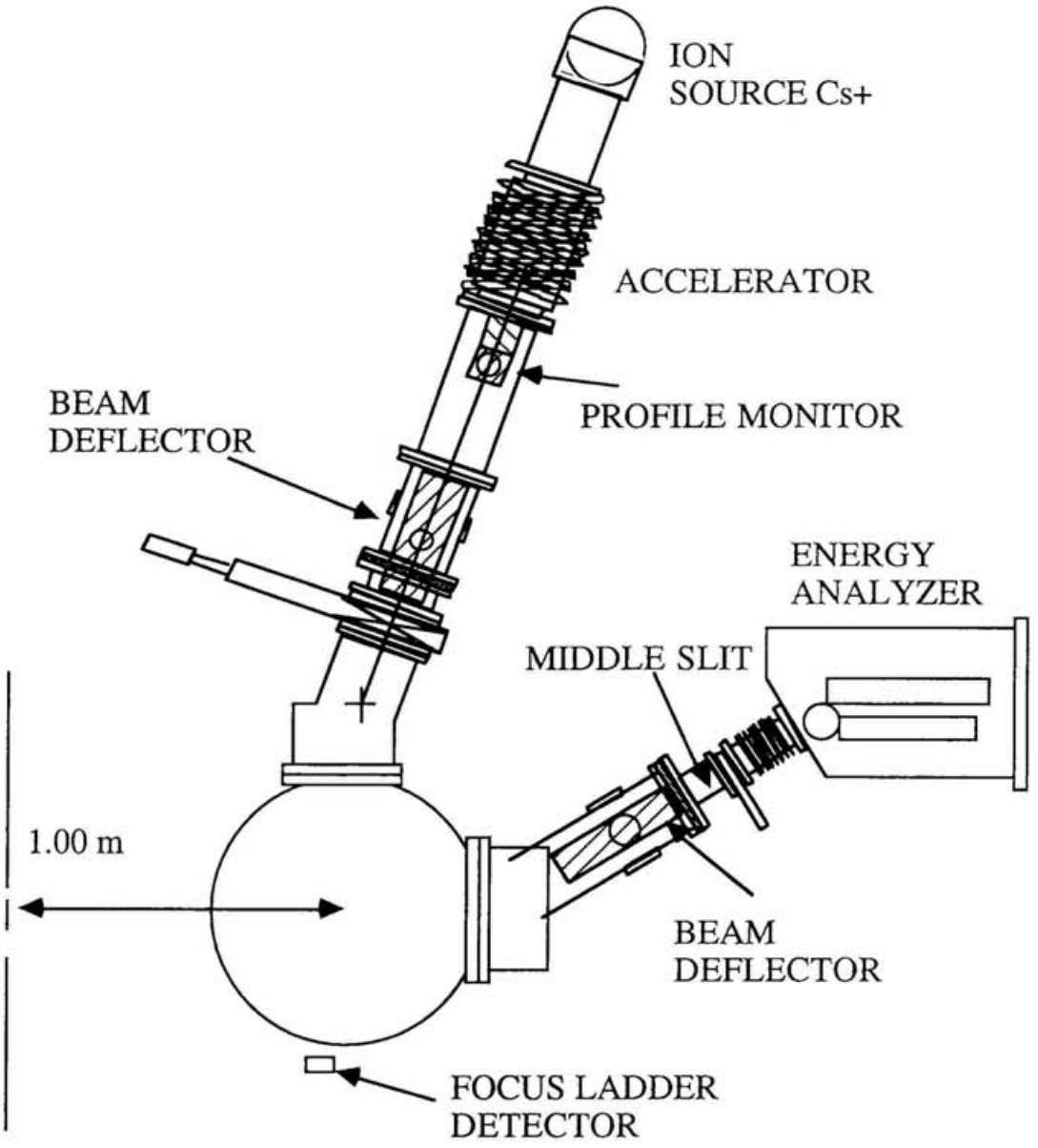

Fig. 2.4: A schematic view of the 200keV heavy ion beam probe on CHS. The beam line on the analyzer side is separated from that on the injector side by 22.5 ° in the toroidal direction.

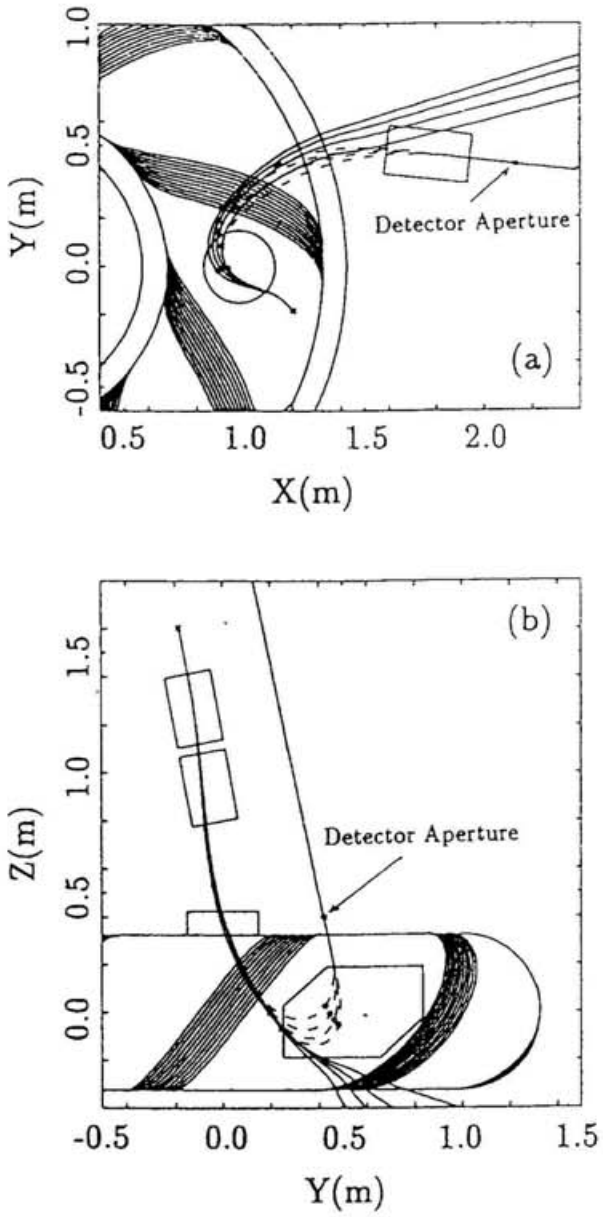

Figure 2.5: Sample beam trajectories in the conceptual design phase.
(A. Fujisawa et al. Rev. Sci. Instrum. 3694 (63) 1992)

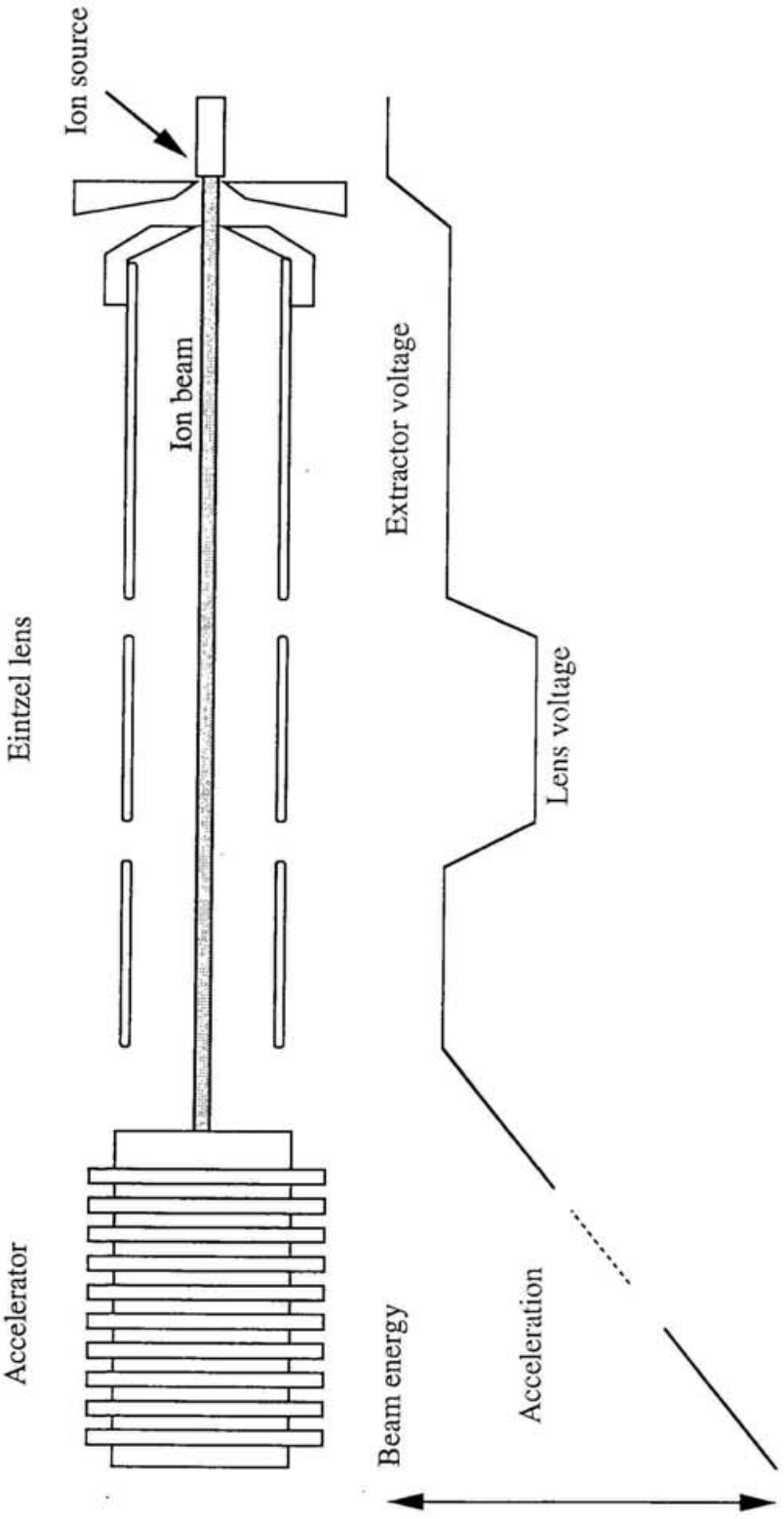

Figure 2.6: Schematic view of beam extraction and focusing system.

2.2.2 Complete beam control system

The CHS HIBP has two sets of beam deflectors to control the primary and secondary ion beams independently, so that the injection angle of the secondary beam into the energy analyzer is kept constant during whole radial scanning [19]. This method makes the observation area wider and improves accuracy in determining the plasma potential. Figure 2.7 shows a diagram of basic elements and the control system installed on CHS HIBP. The beam deflector is an octupole type and eight high voltage amplifiers (Trek 609A-3) are directly connected to each deflector plate (Fig 2.8). The combination of high voltages is determined to produce uniform electric field in the deflector. The magnitude and direction of the electric field can be characterized by the high voltages of two deflector plates, namely, V_1 and V_2 for the primary beam and V_3 and V_4 for the secondary beam, respectively. Then the total beam line is uniquely determined by the combination of four high voltages if the beam energy is fixed. For the typical configuration of magnetic axis R_{ax}=94.9cm and magnetic field strength B=1T, the sweep plate voltages V_1=-568V, V_2=507V, V_3=120V, V_4=-36V for Vb=75keV are required to measure the plasma center[33]. Sets of four sweep voltages for full radial scanning are shown in Fig. 2.9 (a) together with the corresponding observation points as shown in Fig. 2.9 (b).

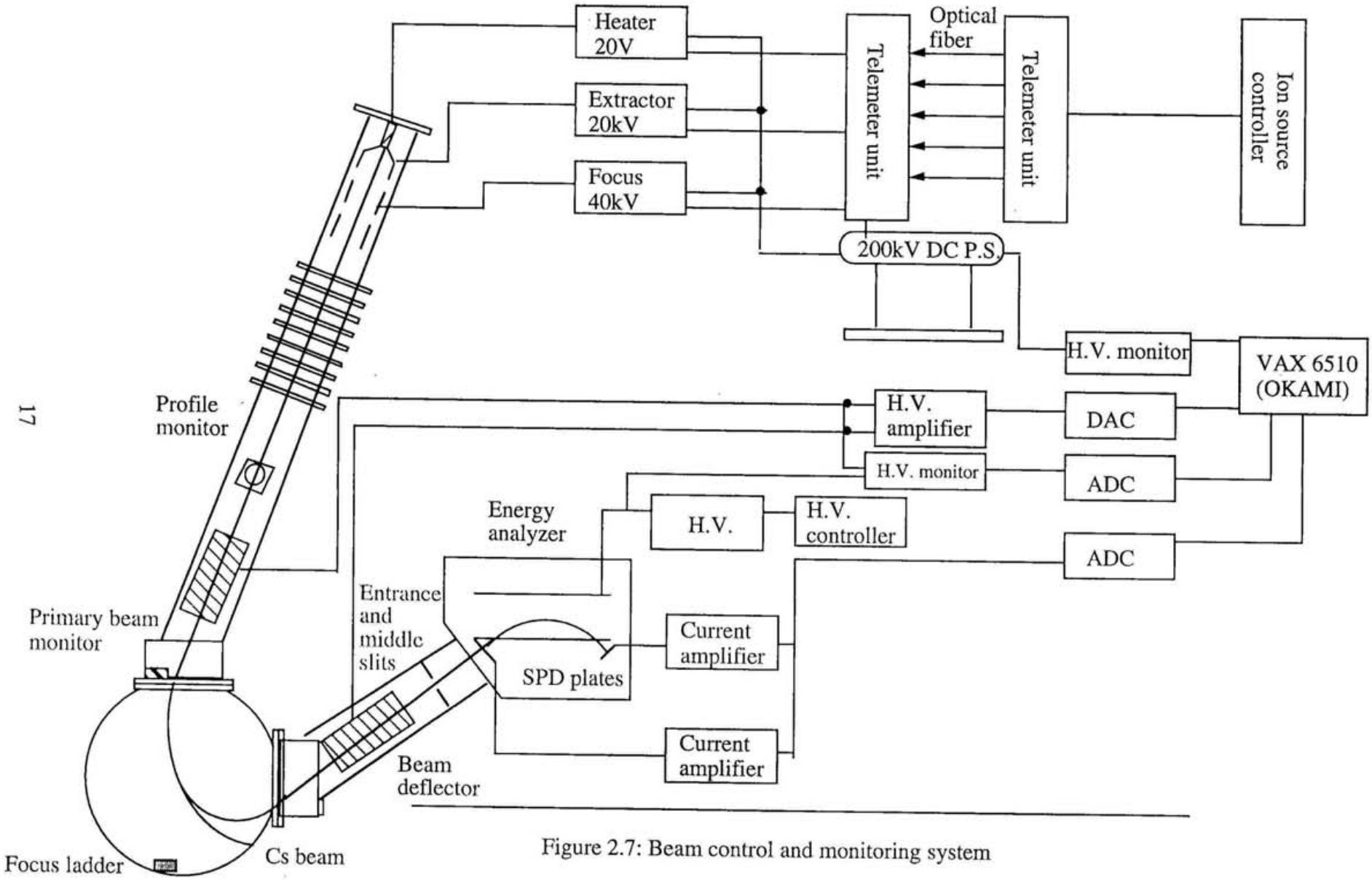

Figure 2.7: Beam control and monitoring system

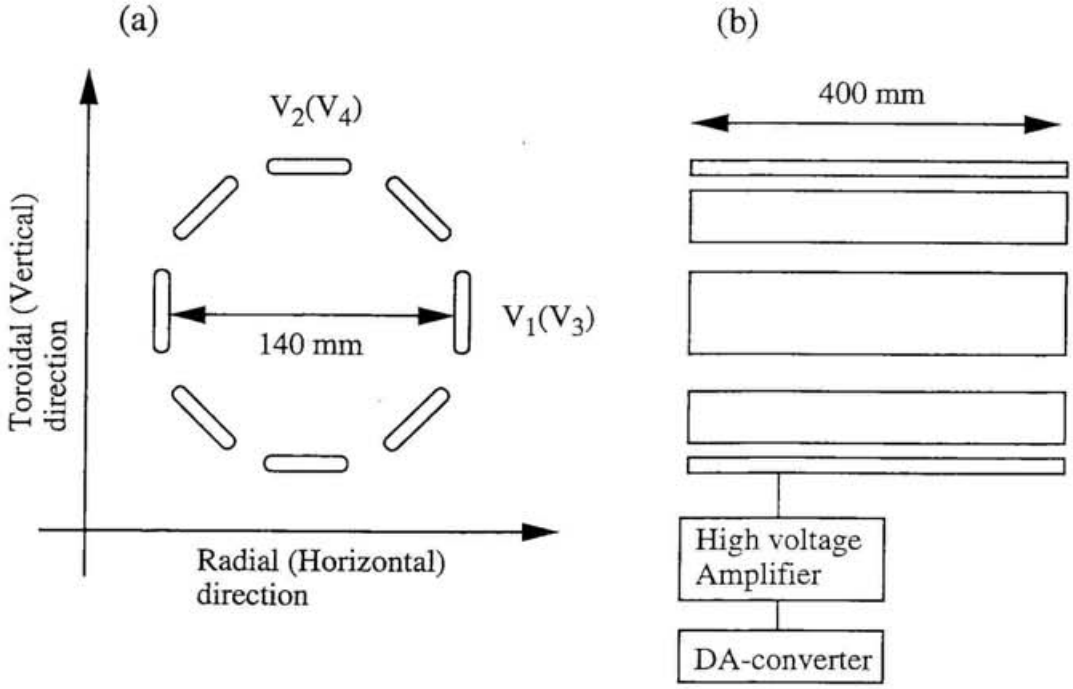

Figure 2.8: A schematic view of the octupole deflector. Dimensions are the same for the primary and the secondary beams.

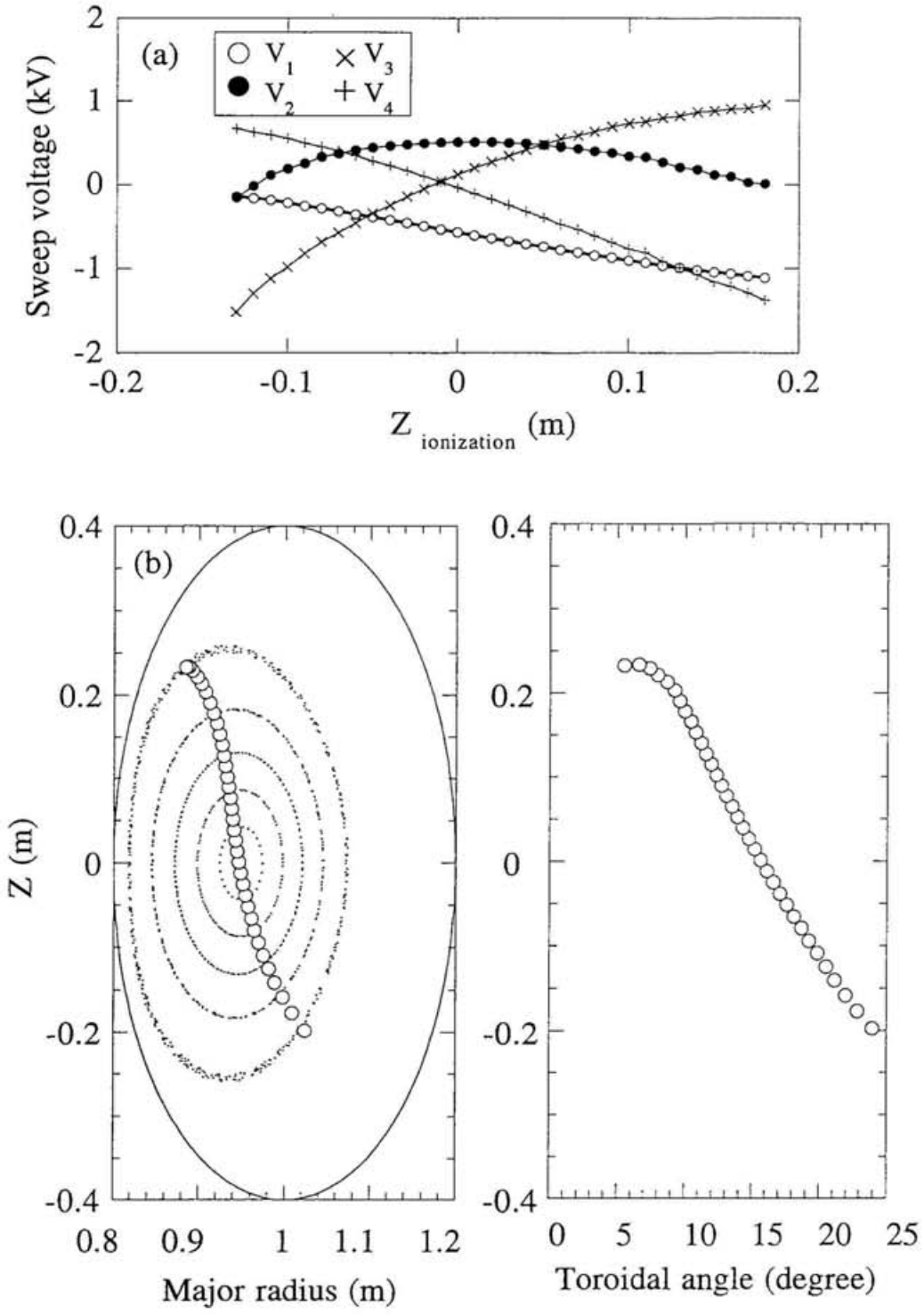

Figure 2.9: (a) A sweep voltage sets and (b) sample positions. (R_{axis}=94.9 cm, B_T=1.0 T)

2.2.3 Energy analyzer

The Proca and Green type energy analyzer (Fig. 2.10) has the second order focusing property for the vertical injection angle[34]. The normalized beam current difference between top and bottom split plates is related with the beam energy W as follows:

$$W = q_s V_A \left\{ \frac{I_T - I_B}{I_T + I_B} F(\theta_I, \alpha) + G(\theta_I, \alpha) \right\} , \qquad (2.1)$$

where V_A is the analyzer voltage, I_T and I_B are the total beam currents on the top and bottom plates, respectively. The functions $G(\theta_I, \alpha)$ and $F(\theta_I, \alpha)$ are given by

$$G(\theta_I, \alpha) = \frac{X_D \tan\theta_I - Y_D}{4\, d \sin^2\theta_I \cos^2\alpha}$$

$$F(\theta_I, \alpha) = \frac{w(\sin\theta_a + \cos\theta_a \tan\theta_I)}{8\, d \sin^2\theta_I \cos^2\alpha} \qquad (2.2)$$

Here, θ_I is the injection angle of the beam into the analyzer, Y_D ($=Y_{D1}+Y_{D2}$) is the total height of drift space, w is the entrance slit width, α is the off center angle as shown in Fig. 2.10, d is the distance between the ground plate and the high voltage plate, and X_D is the distance between the entrance slit and SPD detector[35].

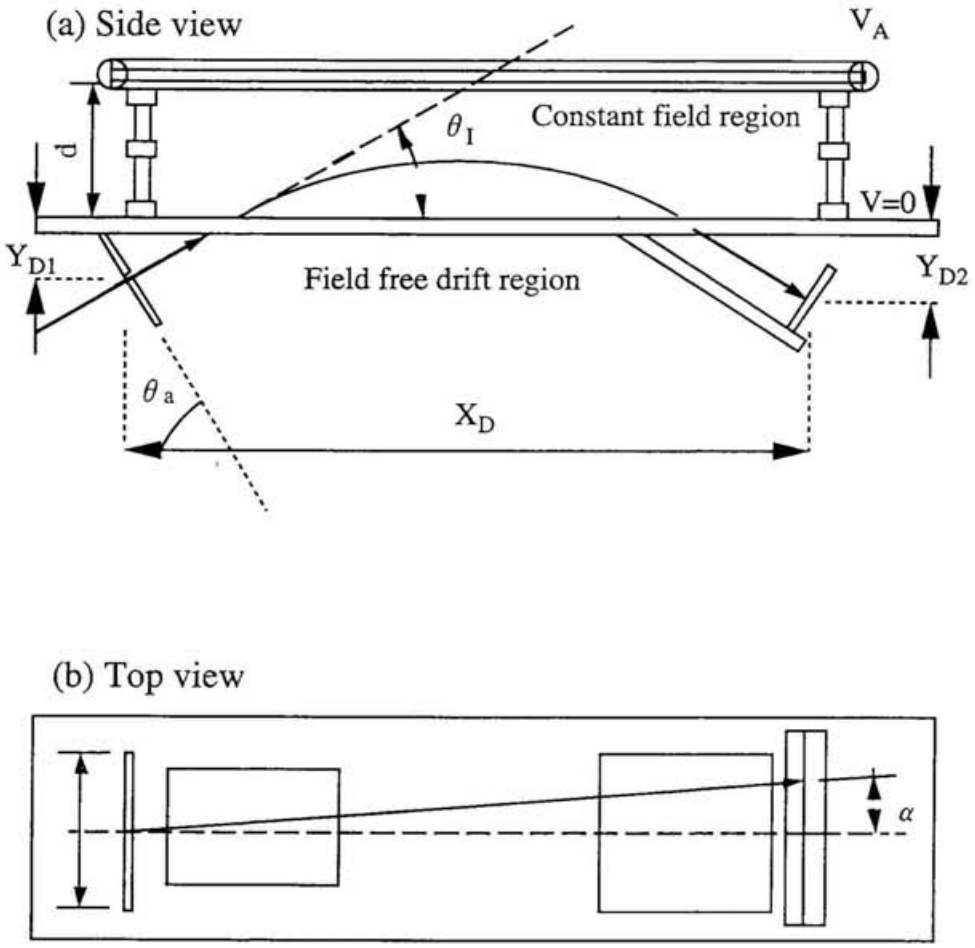

Figure 2.10: A Proca-Green type energy analyzer; (a)top view (b) side view.

The functions $G(\theta_I, \alpha)$ and $F(\theta_I, \alpha)$ of the CHS analyzer are determined to be G~2.45 and F~1.5×10^{-2} by calibration, for $\theta_I=30^\circ$ and $\alpha=0^\circ$. The dynamic range of potential measurement D is given by the analyzer voltage V_A and the F value as

$$D = 2\, q_s V_A F(\theta_I, \alpha) \,. \qquad (2.3)$$

The resolusion of potential measurement is determined by the circuit noise of the current amplifier and is given by the following relation,

$$\delta\phi = 2\, q_s V_A F(\theta_I, \alpha) \frac{I_{noise}}{I_{sum}} \,. \qquad (2.4)$$

In this experiment, w is fixed to be 2 mm and the dynamic range is $\pm$450 V for V_b=75 keV. The minimum detectable potential is less than several volts for typical noise level of I_{noise}/I_{sum}~1%.

The gain of the current amplifier is 10^8 V/A for gas ionization experiments and 10^7 V/A for plasma experiments. The output of the current amplifiers is introduced to CAMAC digitizers with the sampling time of 2 μs.

2.3 Beam line alignment

In the CHS HIBP, an observation point is determined by the combination of four deflector voltages. Since observation points are sensitive to the accuracy of beam line alignment and fringing field of the deflectors, experimental calibration for beam alignment is necessary to verify the accuracy of the total system. A movable detector and a gas ionization method have been used to study beam trajectories[36,37].

2.3.1 A movable detector

Figure 2.11 shows the schematic view of the movable detector (a) and its head shape (b). The detector was at first used for the primary beam detection. The center of the detector head was set at the magnetic axis R_{ax} = 94.9 cm, which corresponds to the typical magnetic configuration in CHS operations. The experiment was carried out at Bt = 1 T. A 75 keV cesium beam was injected from the top port into the CHS chamber. The beam was swept two-dimensionally with different frequencies in the radial and toroidal directions to find two corresponding deflector voltages to hit the detector, and those voltages of V_1=- 480 $\pm$ 240 V and V_2=540 $\pm$ 230 V were obtained respectively (Fig. 2.12). The ambiguity of the sweep voltage set is mainly caused by uncertainty of detector head position. A focus ladder detector placed at the bottom port is usually used to adjust beam focusing. Since the magnetic field itself works as a focusing element, the detector was also used to optimize the beam profile at the magnetic axis.

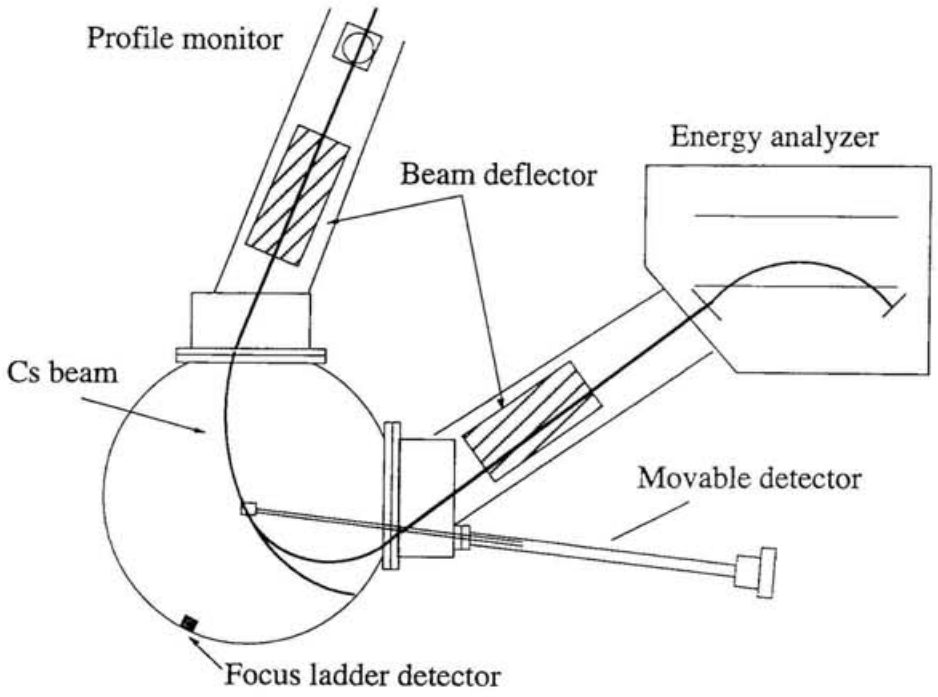

Figure 2.11 (a): Schematic view of the movable detector arrangement.

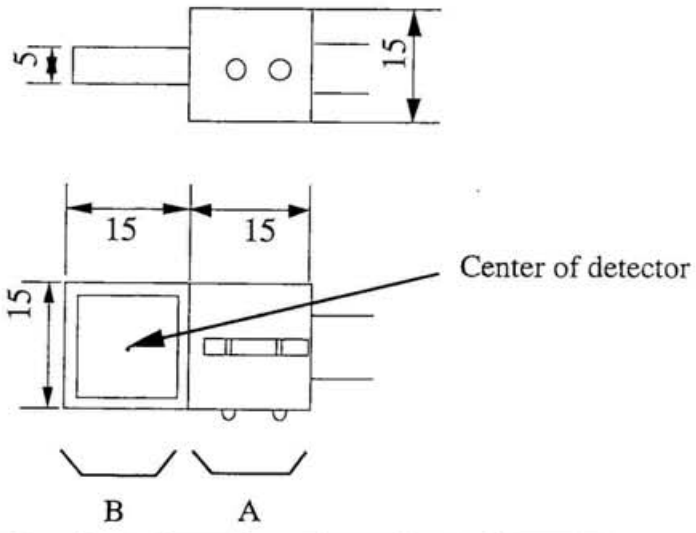

Figure 2.12 (b): Head shape of the movable detector. The current signal presents a single or a double peak depending on the beam sweeping area to be A region or B region, respectively.

It was also examined whether beam focusing is influenced by the presence of helium neutral gas through charge exchange or re-ionization processes of the primary beam. The primary beam current was examined in several gas pressure levels (which was controlled by gas puff duration). As is shown in Fig. 2.13 no serious effect on the beam orbit or beam profile was observed up to the helium pressure of 1×10^{-4} Torr, although the beam intensity was slightly reduced as the gas pressure increased. This result guarantees the usefulness of the gas ionization method described below.

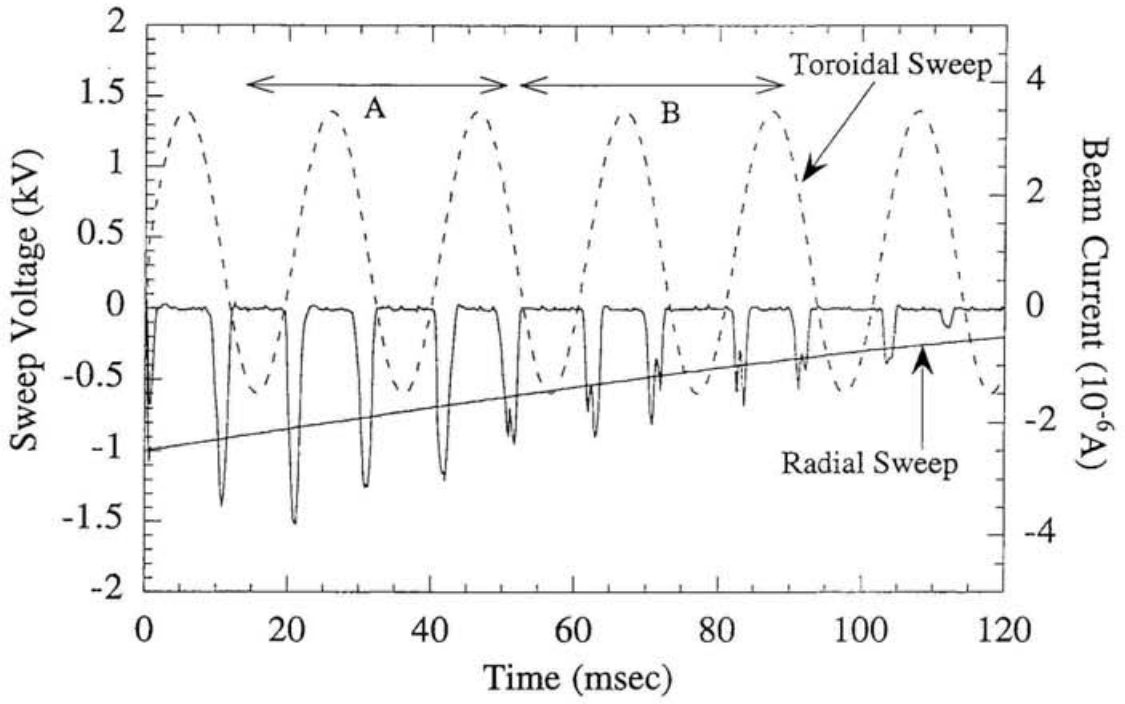

Figure 2.12: Beam current on the movable detector in the beam sweep experiment.

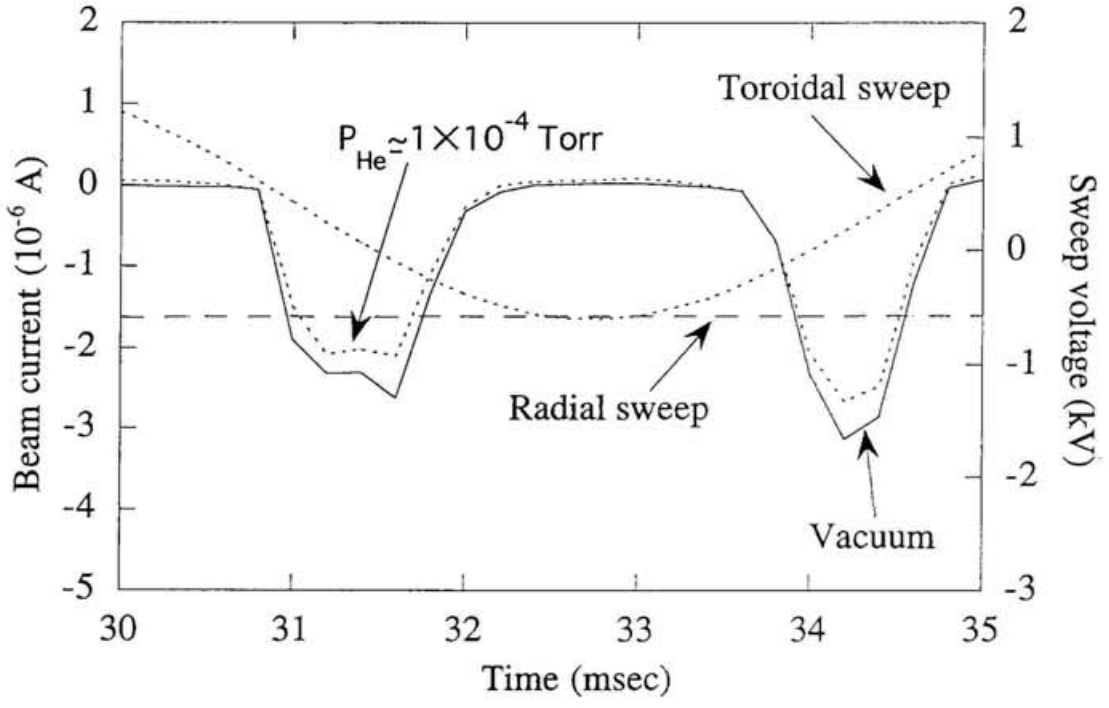

Figure 2.13: Beam current on the movable detector in various pressure levels.

The detector was then used as a biasing electrode to determine the set of deflector voltages for the secondary beam for observing plasma center. A schematic view of calibration procedure is shown in Fig. 2.14. Uniform background helium gas was supplied by gas puffing for about 90 ms. The secondary beam created with gas ionization process at the center of the biased detector has an additional energy same as the electrode potential, and the energy analyzer can identify these secondary ions. In the experiment, the bias voltage up to 900 V was applied to the detector and the beam energy was analyzed by sweeping the secondary beam, while the primary beam was fixed to pass through the center of the detector. Secondary beams are created everywhere along the primary beam trajectory, but their energies are different depending on the ionization position. Figure 2.15 shows the energy change of the secondary beam as a function of the deflector voltages in the analyzer side. The energy change was determined by the following relation:

$$\phi_{gain} = q_s V_A F(\theta_I, \alpha) \left(\underbrace{\frac{I_T - I_B}{I_T + I_B}}_{\text{(with bias)}} - \underbrace{\frac{I_T - I_B}{I_T + I_B}}_{\text{(without bias)}} \right) , \qquad (2.5)$$

where ϕ_{gain} is the energy change of secondary ions, I_T and I_B are total beam currents of top and bottom plates respectively. The maximum energy change was observed at the deflector voltages of $V_3 = 300 \pm 120$ V and $V_4 = 50 \pm 120$ V for horizontal and vertical deflectors, respectively. Taking account of averaging over finite sample volume [38], we concluded that this set of deflector voltages corresponds to the observation point at the magnetic axis. The difference between the applied potential on the detector head and the observed beam energy change is not explained at the moment. Since the supporting

rod for the detector head and the CHS vacuum chamber with complicated structure have a grounded potential, the space potential distribution near the detector head cannot be calculated analytically. Improving the detector structure with a simple grounded boundary or a detailed calculation of space potential distribution is necessary to avoid such ambiguity. Reducing sample volume by improving beam focussing will also help.

The result was compared with the trajectory calculation and good agreement was obtained as shown in Fig. 2.16 (a) and 2.16 (b).

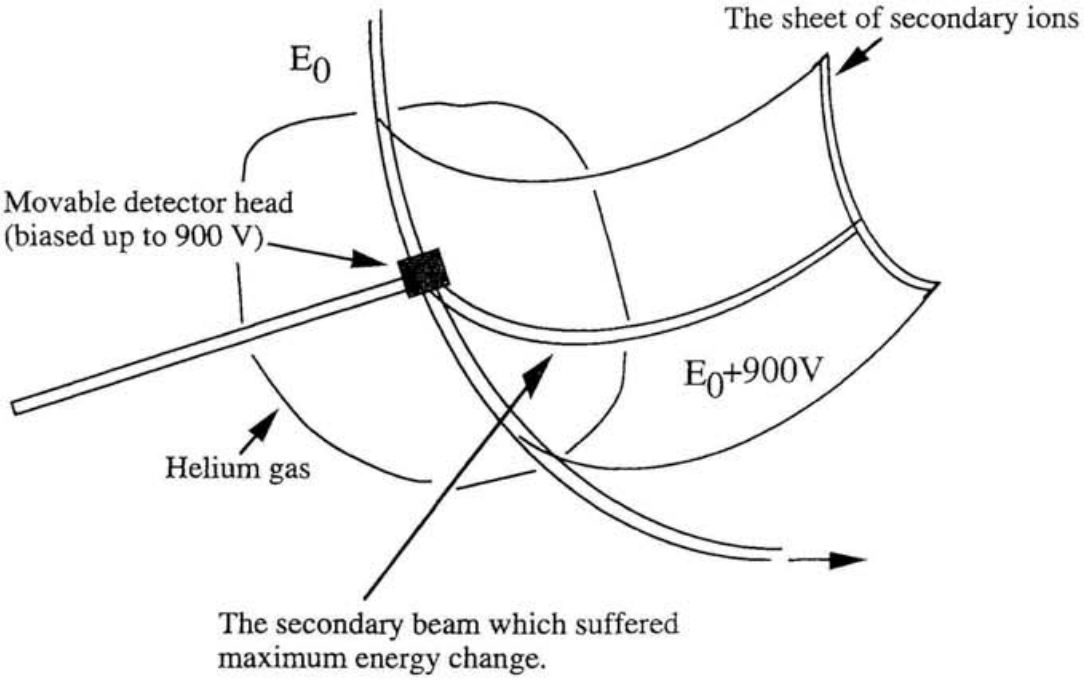

Figure 2.14: Principle of calibration method to determine the sweep voltage set in the secondary beam line.

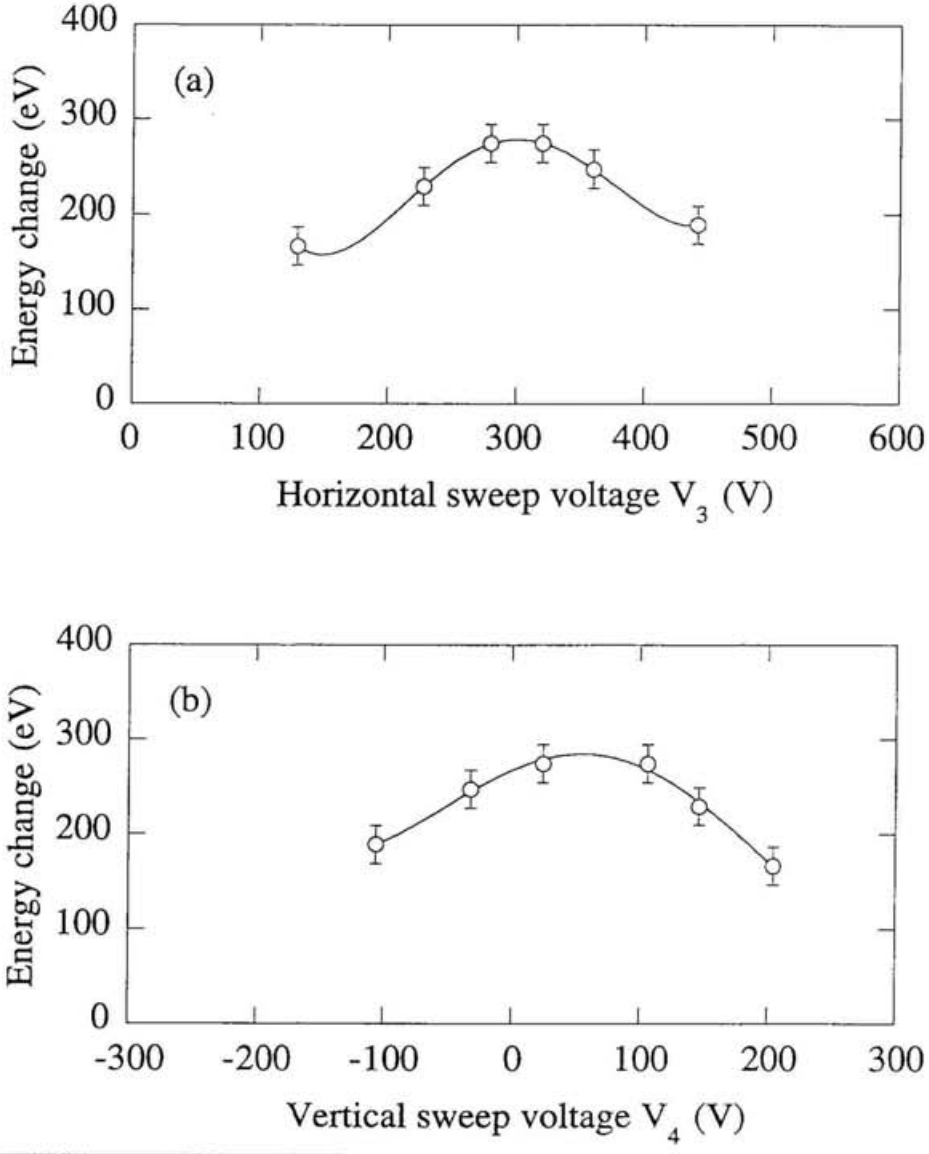

Figure 2.15: Energy change of secondary beams for (a) horizontal and (b) vertical sweep voltages.

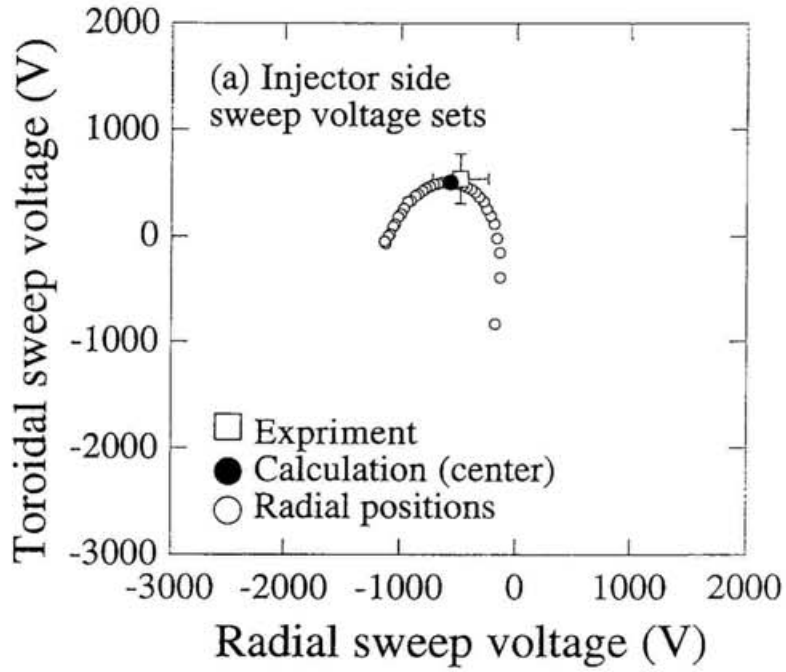

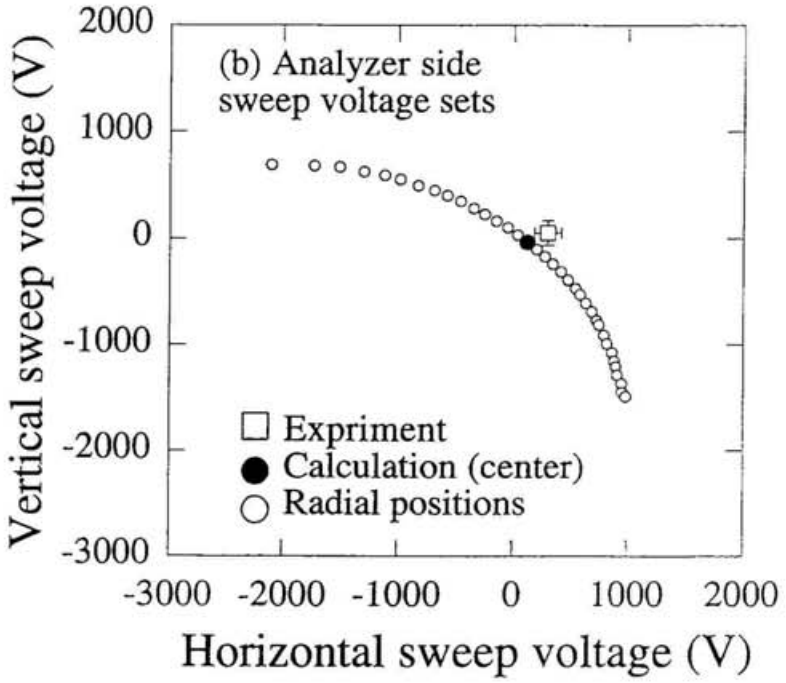

Figure 2.16: Sweep voltage sets which were determined by the movable detector. Solid lines and circles are from trajectory calculation.

2.3.2 Gas ionization method

In order to confirm the sets of deflector voltages for observation points at different plasma radii, the gas ionization method was used. The primary beam at the energy of 75 keV is injected into the CHS chamber filled with a helium gas at the pressure of 1×10^{-4} Torr. The magnetic axis and the magnetic field strength are R_{ax}=94.9 cm and B_t=1.0 T, respectively. The secondary beam is produced by ionization through collisions with helium neutrals, and is introduced into the energy analyzer. Since the neutral gas has no electric potential, the secondary beam should not undergo a change in energy. Combination of four deflector voltages are preprogrammed based on the trajectory calculation, and full radial scanning is carried out during one shot. Although the ionization cross section is small in this range of beam energy, the signal level is large enough for the purpose. As is shown in Fig. 2.17 (a), the normalized current signal balances between top and bottom, and left and right plates signals are kept constant during radial scanning. This result suggests that the programmed sweep voltage sets give proper sample positions along the radial scan line. It is noted that the gas ionization method has another advantage that the sample volume is automatically calibrated because the signal intensity is proportional to it. The sum signal of the secondary beam current is shown in Fig. 2.17 (b). The sample volume is larger on the plasma upper side.

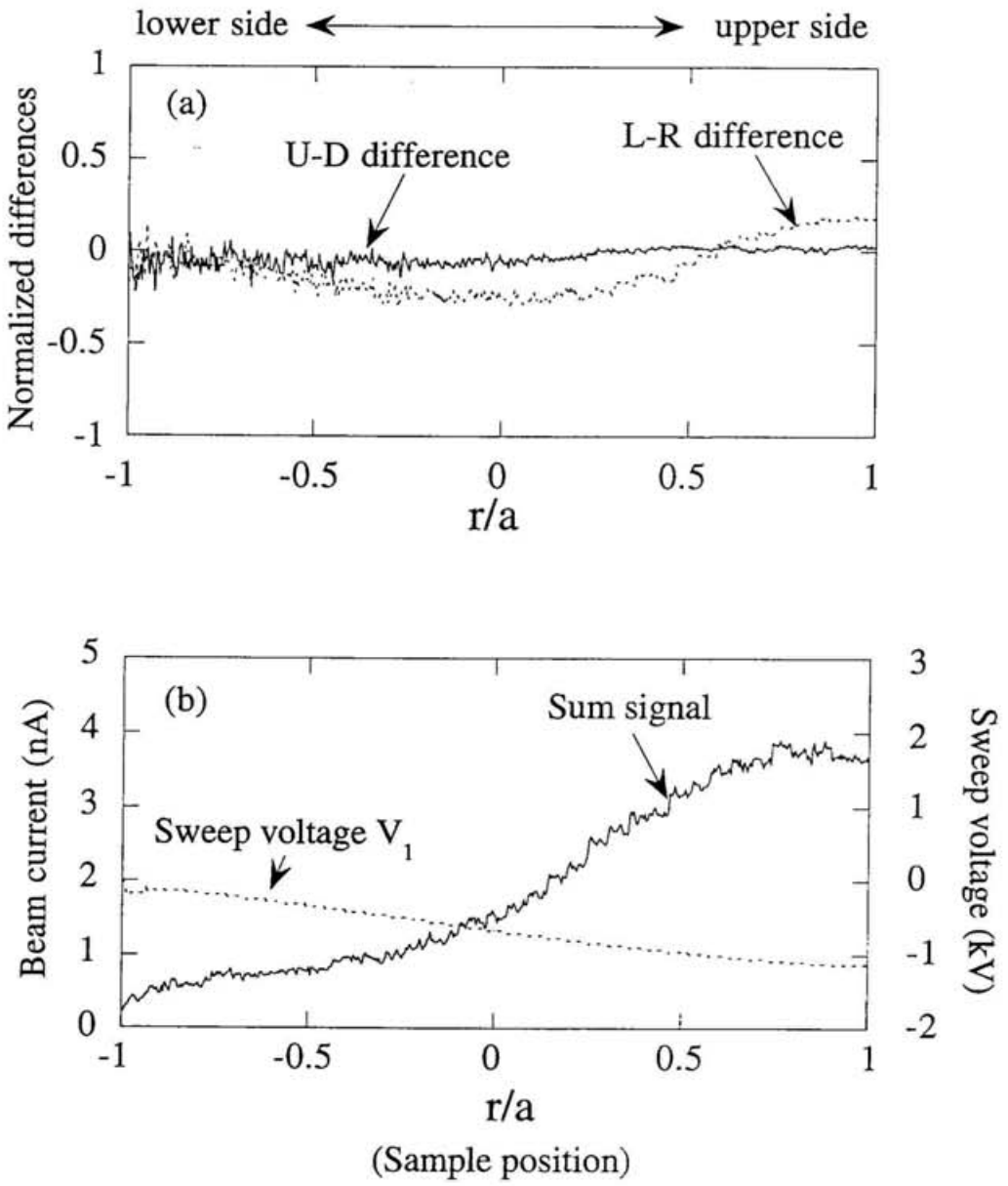

Figure 2.17: (a) Nomalized signal difference (top and bottom, left and right).
(b) Sum signals for each observation points. (B_{axis}=94.9 cm, B_T=1.0 T)

Chapter 3

Measurement

3.1 MHD burst mode

In the Compact Helical System (CHS), magnetic fluctuations have been studied by the use of poloidal and toroidal arrays of magnetic probes[39-42]. It is found that the fluctuation modes depend on the magnetic configuration, beta value, direction of beam induced current during NBI heating, and so on. Among these fluctuations, periodic, burst-type m/n=2/1 (m: poloidal mode number, n: toroidal mode number) modes observed in a low-β, NBI (co-injected) plasma have shown the strongest activity. The oscillation appears, typically every 4 milliseconds, and its frequency generally decreases from 40kHz to 15kHz during a growing phase. The mode is considered to be an interchange instability. However, the mode propagates initially in the ion diamagnetic drift direction but reverses the direction (to the electron diamagnetic drift direction) in the decaying phase.

In this experiment, HIBP is applied to study internal structures of the burst-type MHD oscillations. The experiments are carried out in a low beta NBI plasma. The position of the magnetic axis and the magnetic field strength are 0.92 m and 0.9 T, respectively. This is a typical configuration where the burst-type mode is observed. In this configuration, the q=2 surface is unstable from the Mercier

criterion. The plasma is initially produced by the second harmonic electron cyclotron heating (ECH, 53.2GHz) or ion Bernstein wave (IBW, 7.5MHz) heating, and then neutral beam (NB) is injected (co-injection). The port through power is 0.85 MW. The fueling gas and the injected beam are both hydrogen in this experiment.

Figure 3.1 shows a time evolution of low-β, neutral beam (NB) injected discharge. The line averaged electron density $\overline{n}_e$ is kept low at around $1.7\times10^{19}m^{-3}$ by gas puff control and the diamagnetic beta value is constant at 0.2% during the discharge. Two types of burst modes appear in different phases of the discharge. The first type appears in the initial phase of discharges, where the beam driven plasma current is low (~4 kA), and repeats simple growth and decay in a rather short period. The second type appears in the later phase of discharges, where the plasma current is higher, accompanying a low frequency damping oscillation with longer burst period. Here we concentrate our study on the second type oscillation. Figure 3.2 and figure 3.3 show the variation of oscillation frequency and mode propagation directions during a burst cycle. The frequency decreases from 20kHz to 10kHz during the growing phase, and the mode is propagating in the ion diamagnetic direction. On the other hand, the mode in the decaying phase is propagating in the electron diamagnetic direction with almost constant frequency of around 5 kHz. Those results are basically consistent with the previous experimental studies.

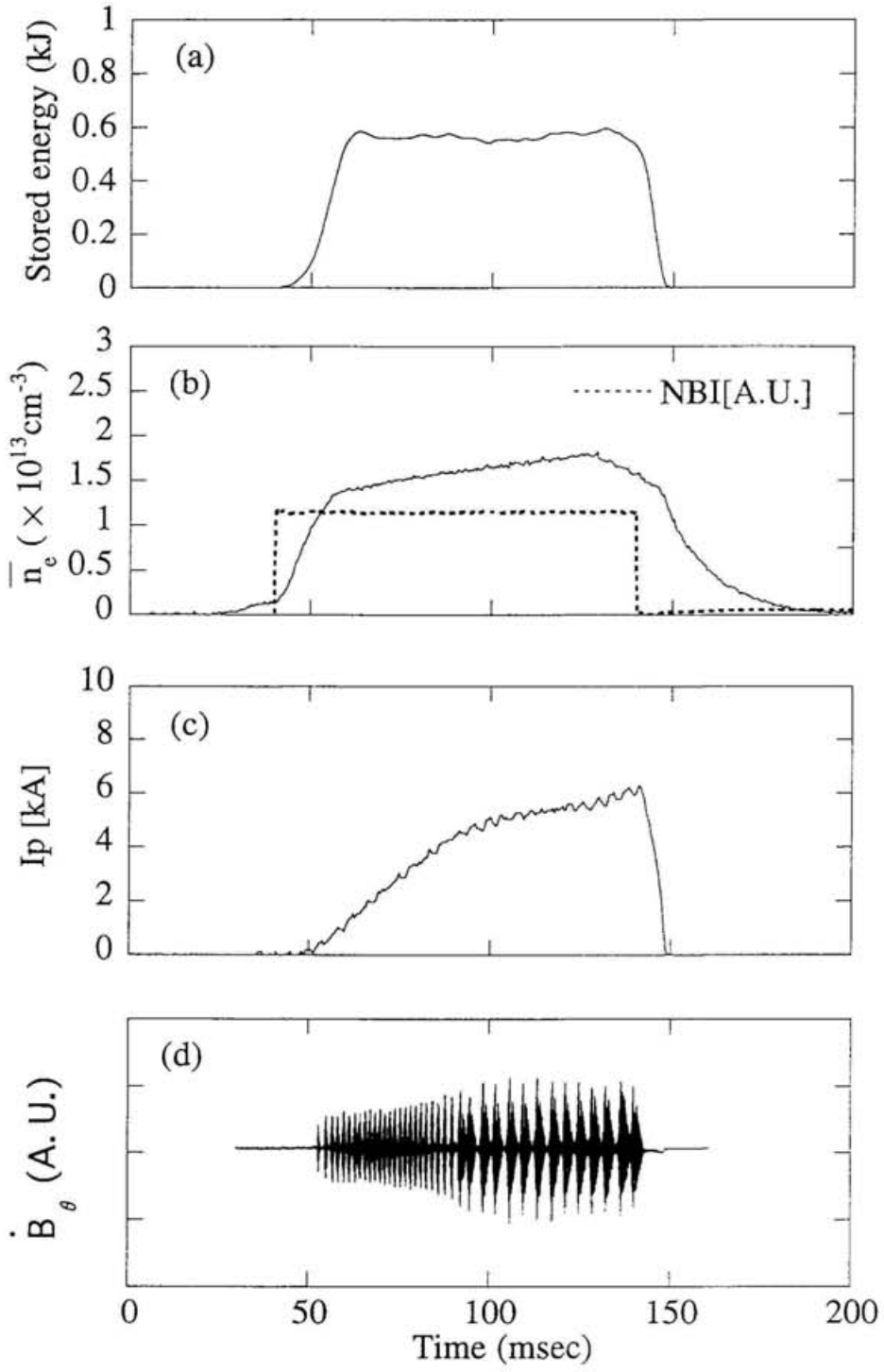

Fig. 3.1: Time evolution of low beta NBI discharge: (a) diamagnetic stored energy;
(b) line averaged electron density;
(c) total plasma current (beam drien current plus bootstrap current);
(d) fluctuation signal of a magnetic probe.

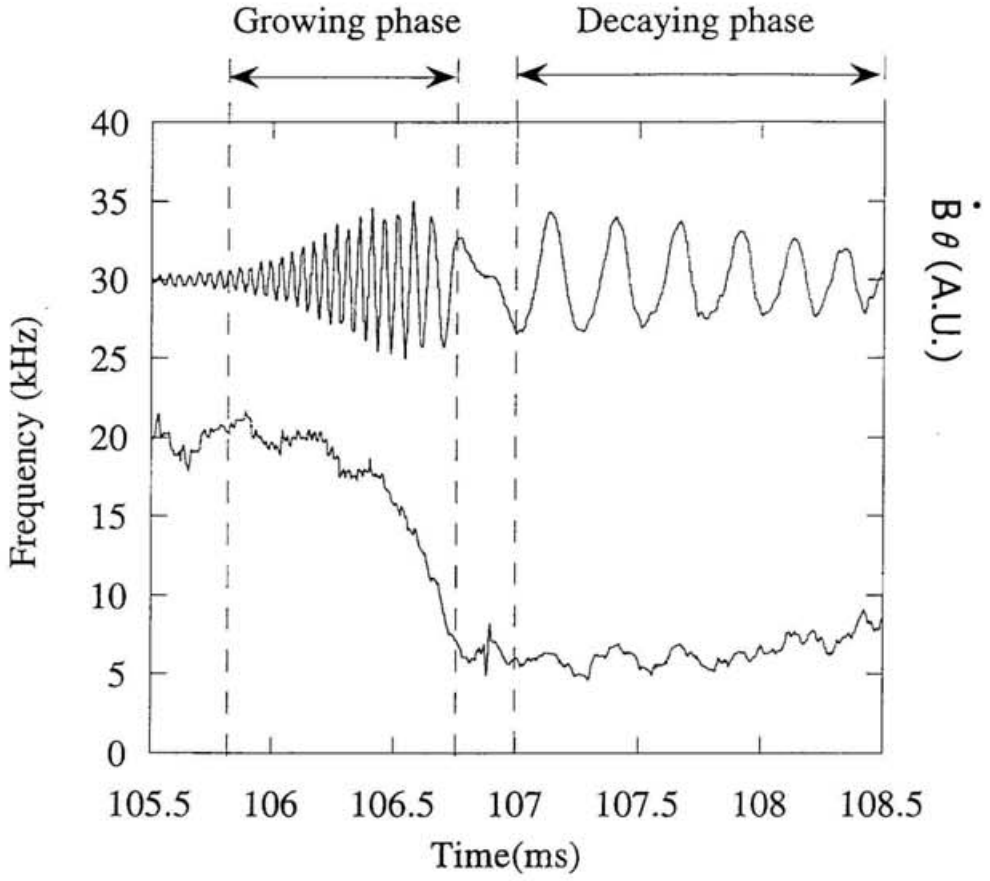

Fig. 3.2: Expanded view of the second type burst mode.
Lower trace shows the time variation of the oscillation frequency.

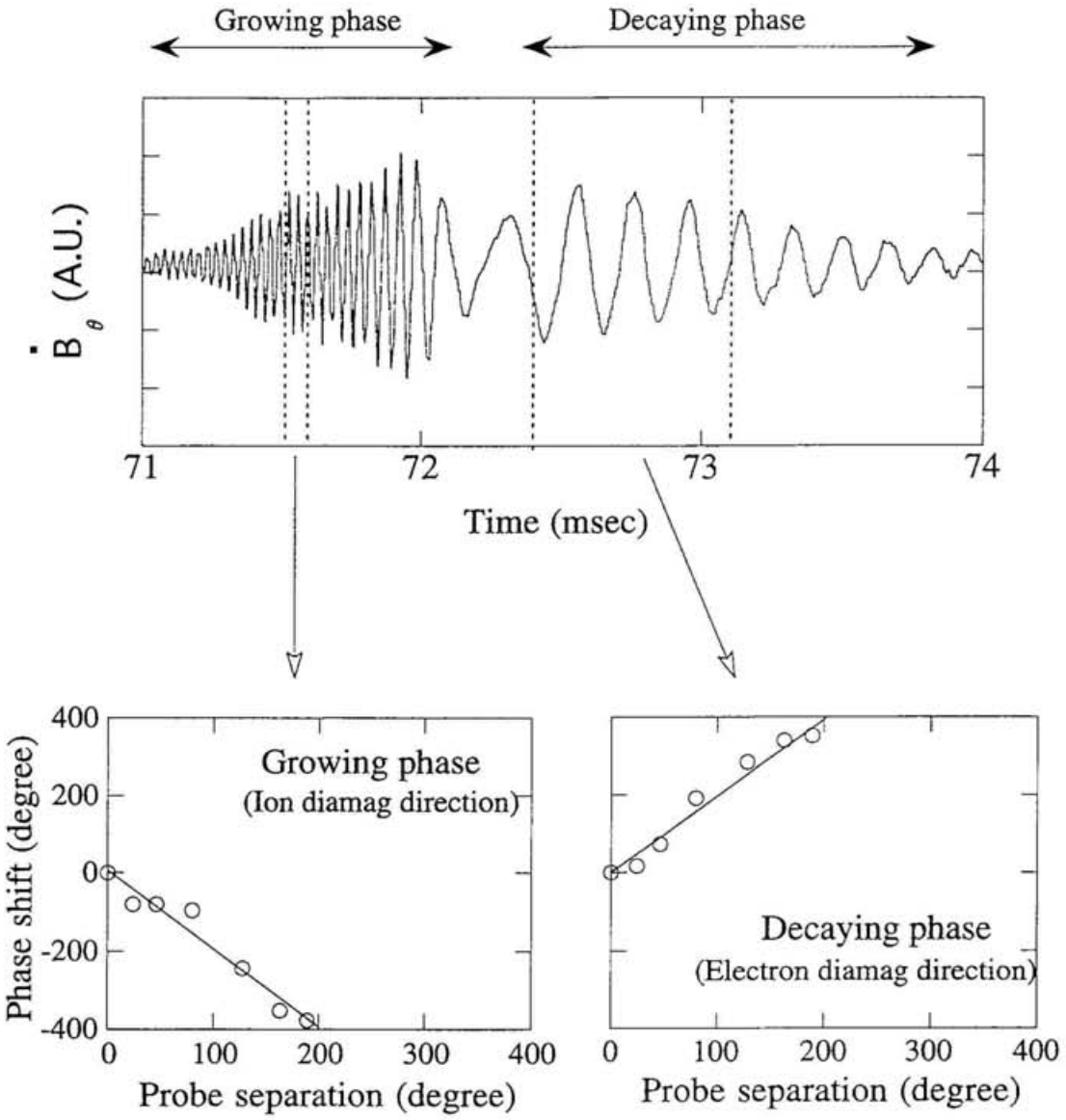

Figure 3.3: Mode propagation analysis with magnetic probe data.
The mode propagates in the ion diamagnetic drift direction in the growing phase and the electron diamagnetic drift direction in the decaying phase.

3.2 HIBP measurements

3.2.1 MHD fluctuations

Figure 3.4 shows the time evolution of the HIBP data where obsevation points are switched every 18 msec. Figure 3.5 (a) and (b) show three kinds of combinations of sample SPD signals, namely, the normalized top-bottom (T-B) difference, sum of the secondary beam current and the normalized left-right (L-R) difference during one MHD burst cycle, together with the magnetic probe signal. The normalized minor radius ρ (=r/a) of sample position is about 0.4 in these figures. It is shown that all three SPD signals are correlated well with the magnetic probe data, except that the fluctuation in the normalized T-B difference in the decaying phase is drastically suppressed. The normalized T-B differences for different radial positions and resultant spatial distributions of the fluctuation level are shown in Fig. 3.6 (a) and (b), respectively. Although the data points are taken shot by shot, the amplitude can be compared each other, because the fluctuation is very reproducible. Actually the amplitude variation in the magnetic probe signals is less than 5 %. The fluctuation level is high at around ρ=0.6, where the q=2 rational surface is located. It is also shown that the fluctuations in the normalized T-B difference are suppressed everywhere in the decaying phase. The normalized L-R difference presents the similar property with the normalized T-B difference. Figures 3.7 (a) and (b) show the time evolution of the sum signal fluctuations (I_{sum}) at several sample positions and the spatial distributions of fluctuation level, respectively. Fluctuation level is higher outside the q=2 surface during the whole burst period.

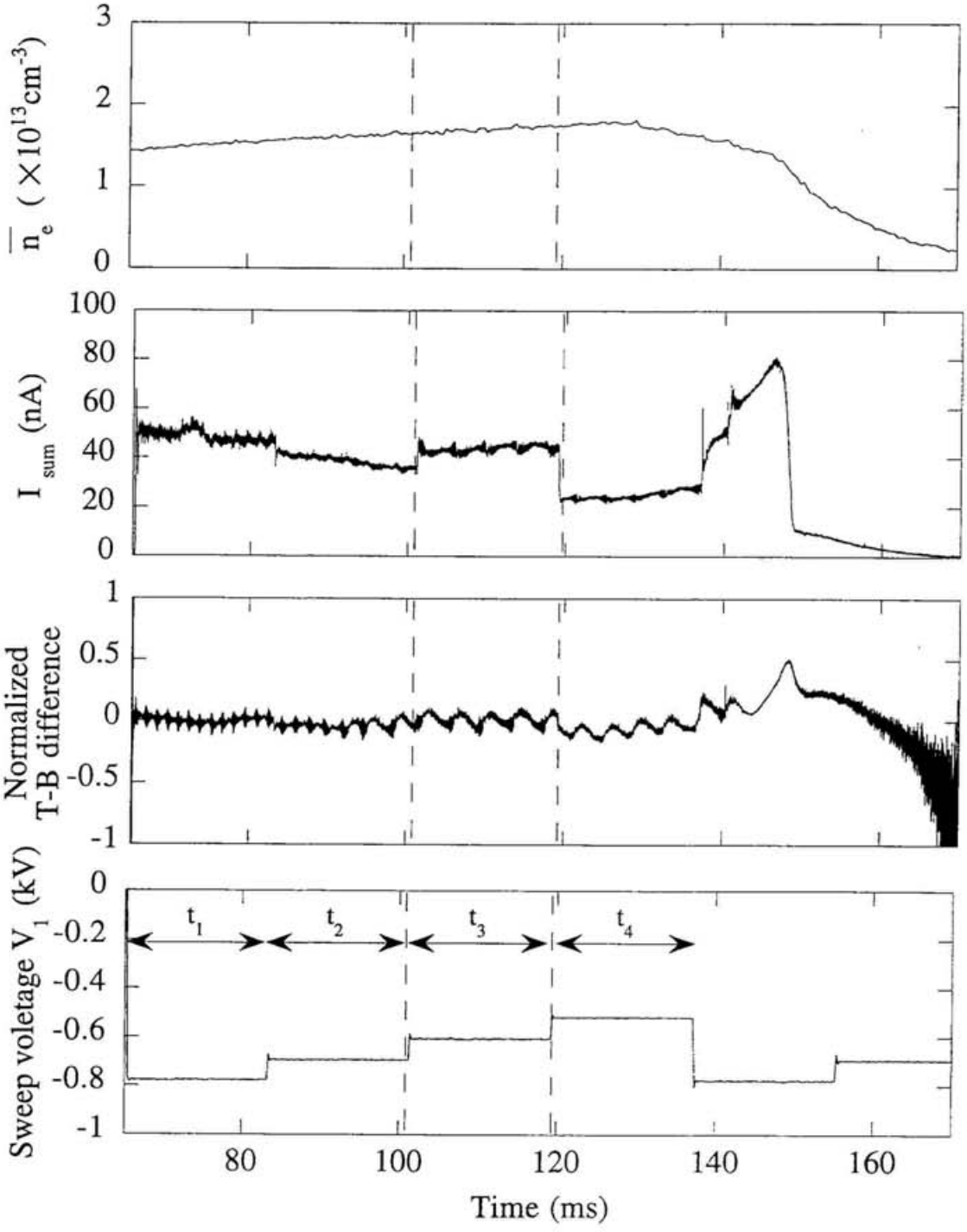

Figure 3.4 : Time evolution of the line averaged electron density, sum of the secondary beam, normalized T-B difference, sweep voltage (V_1). The third period (t_3) data are used in the analysis.

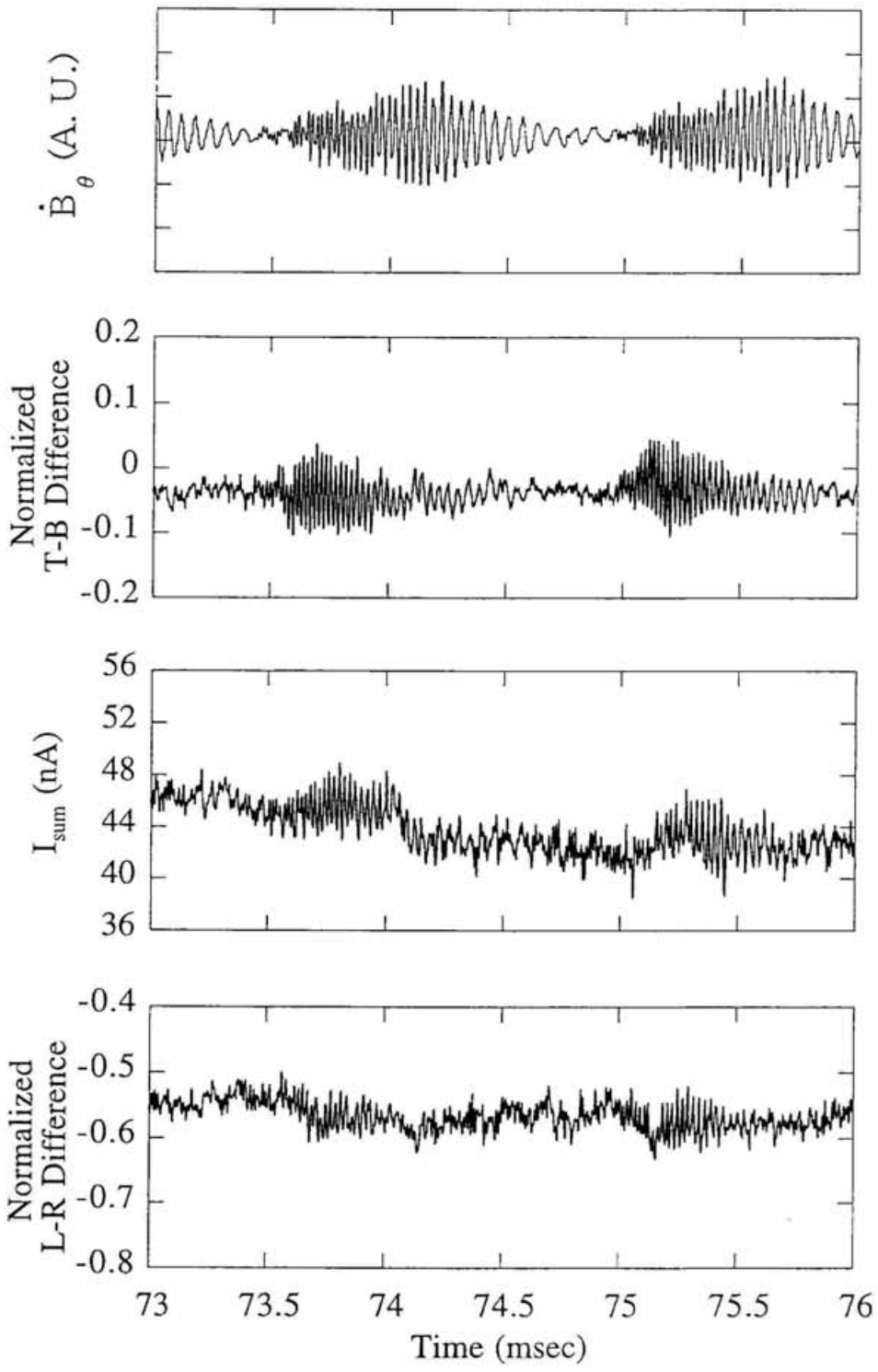

Fig. 3.5 (a): Typical time variation of the normalized top-bottom difference, the current sum and normalized L-R difference in the burst-type MHD instability (the first type).

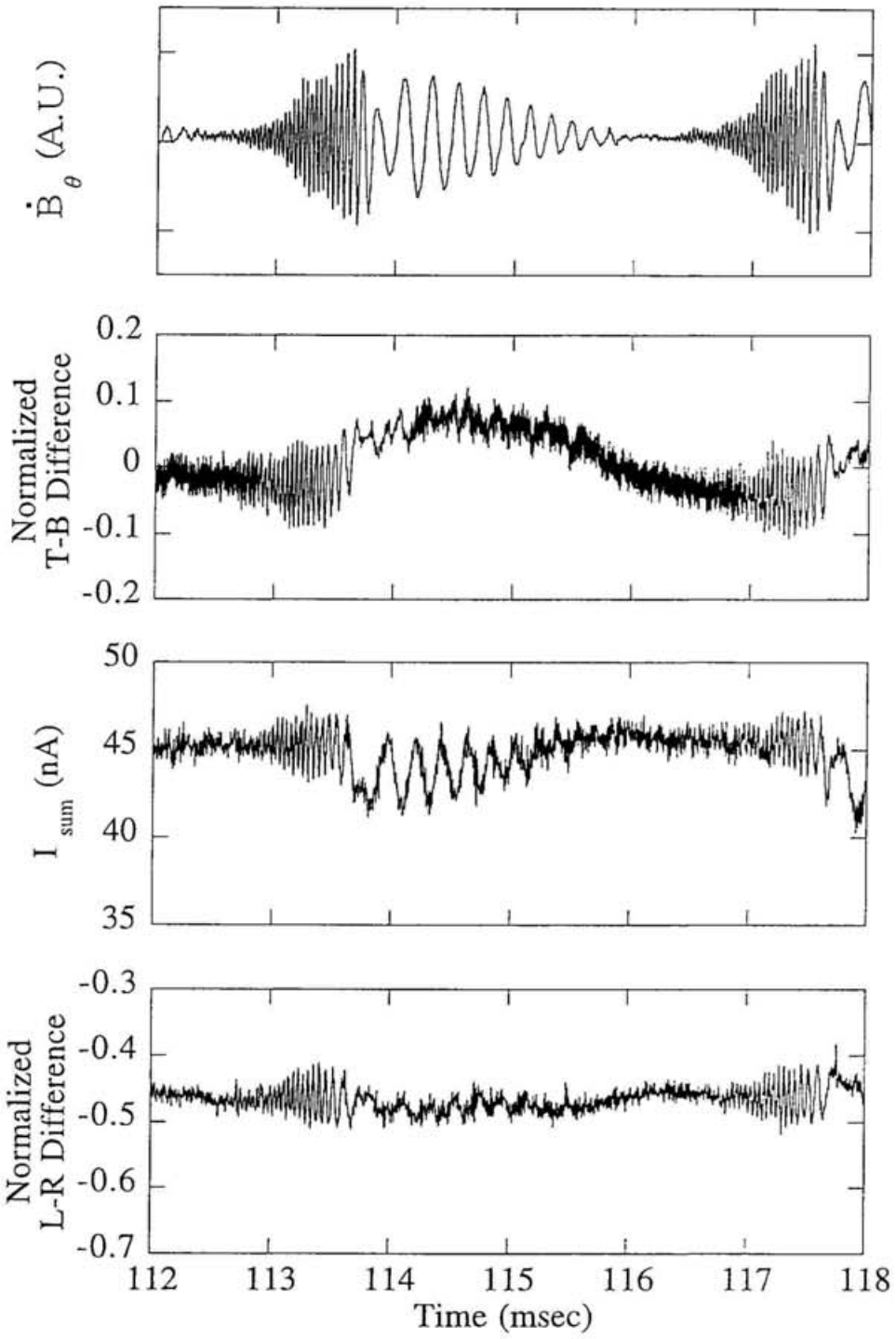

Fig. 3.5 (b): Typical time variation of the normalized T-B difference, the sum and the normalized L-R difference in the burst-type MHD instability (ρ =0.4).

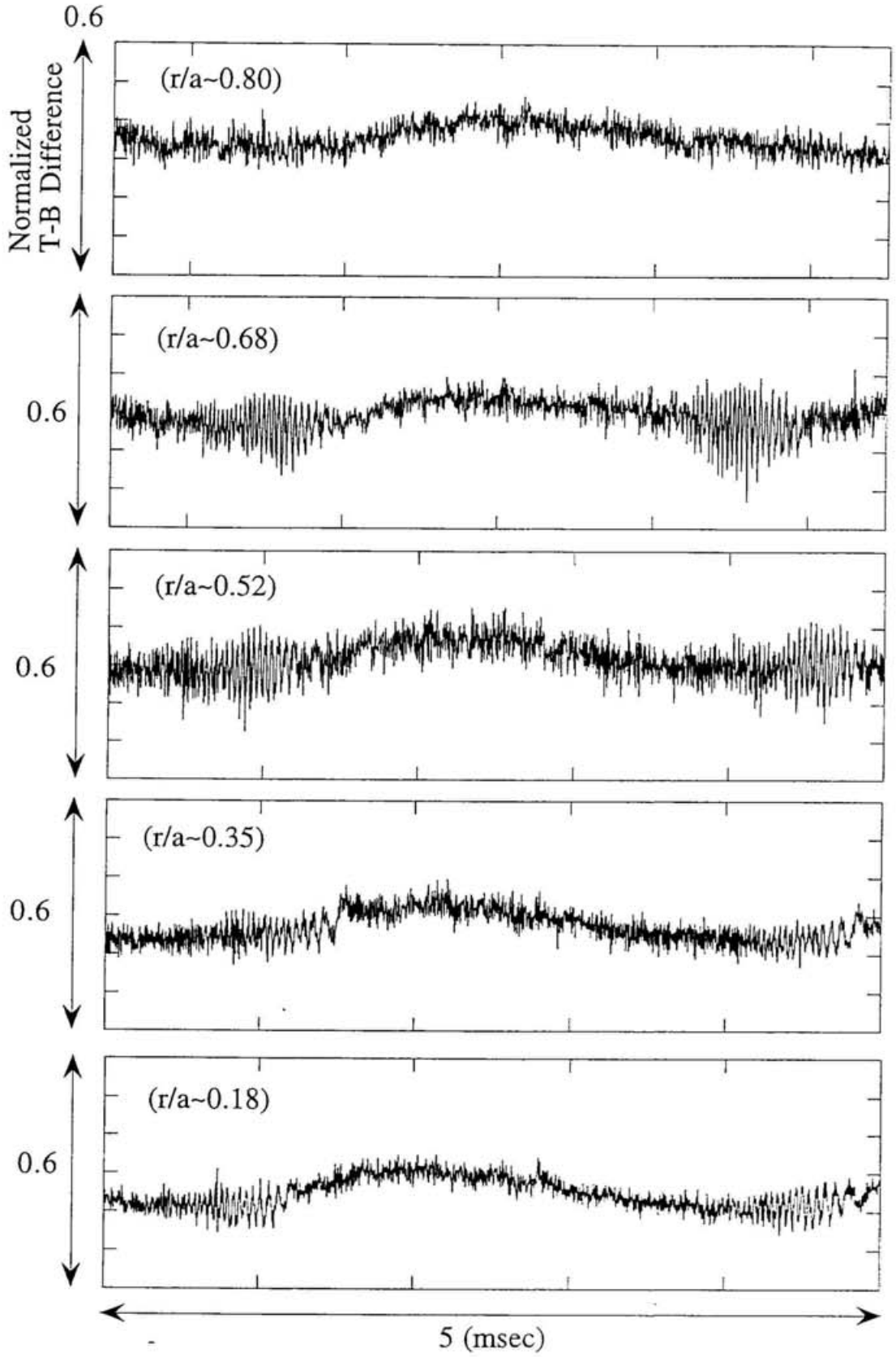

Fig. 3.6 (a): The normalized top-bottom difference at several radial positions.

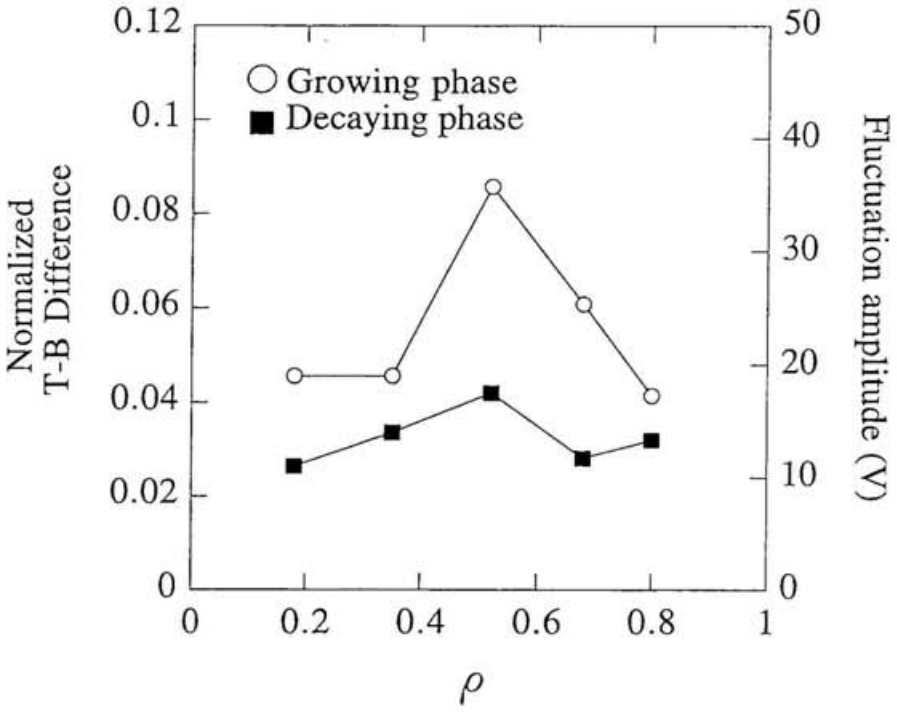

Figure 3.6 (b): Normalized T-B difference for each sample positions. Vertical scale on the right hand side is the fluctuation levels.

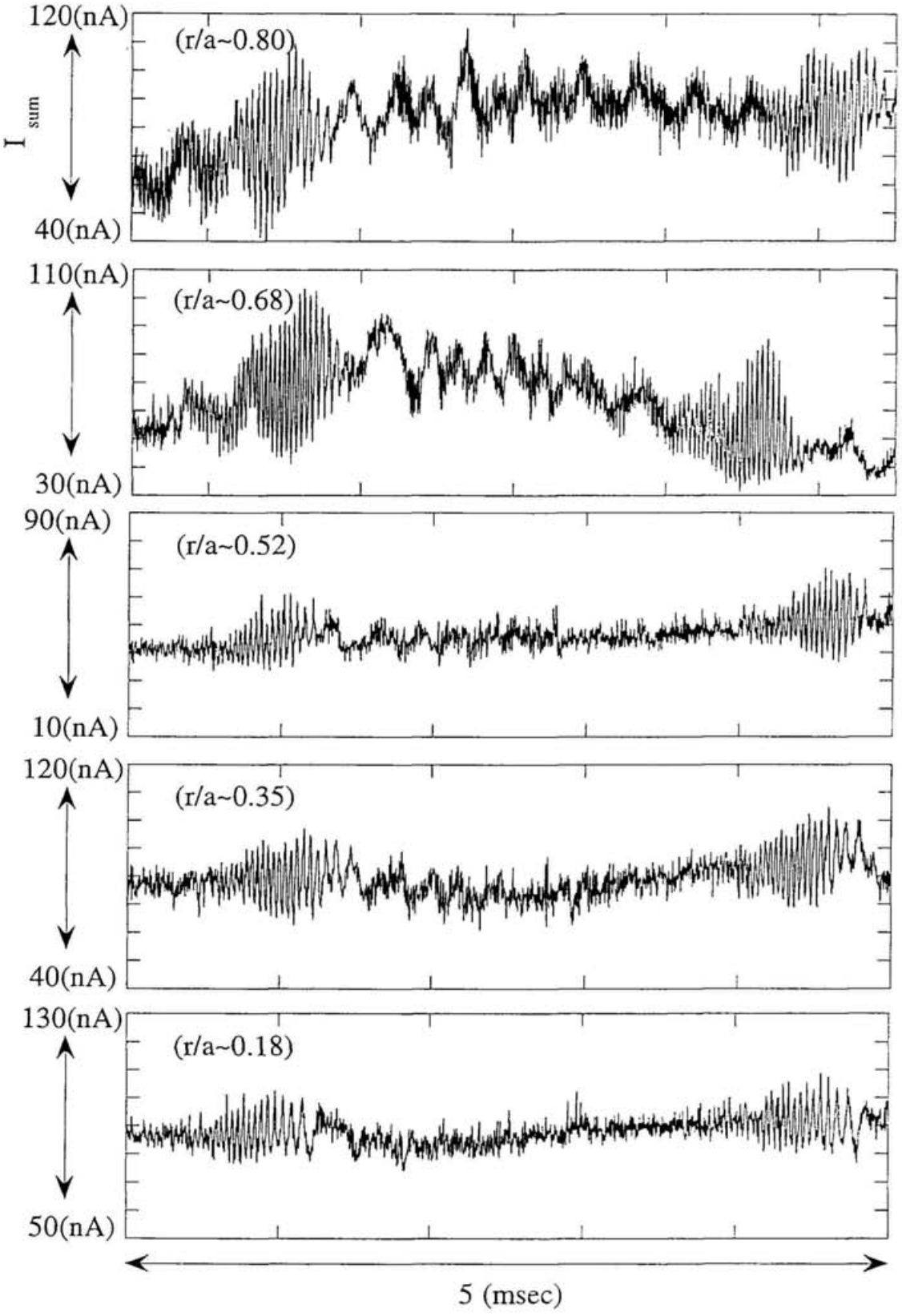

Fig. 3.7(a): The sum signal at several radial positions.

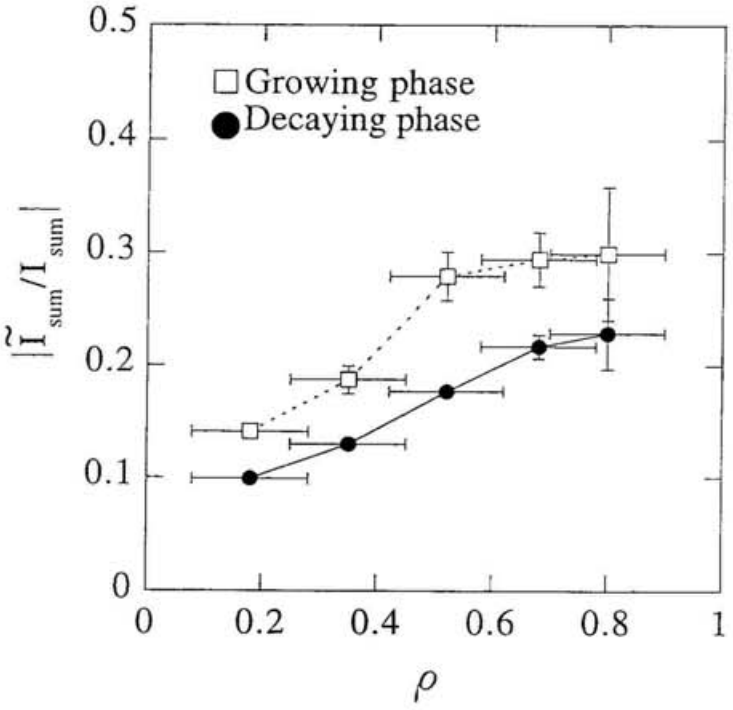

Figure 3.7 (b):Normalized amplitudes of sum signal fluctuations for several observation points.

3.2.2 Electrostatic potential

It is possible to deduce the radial electric field from the potential profile. The electric field has been measured in similar discharges, where continuous radial scanning during one shot has been carried out. As is shown in Fig. 3.8, an NB injected plasma usually presents a negative electric potential all over the plasma radii[33,43,44]. Therefore the $E_r \times B_\phi$ motion (E_d:radial electric field, B_ϕ:toroidal component of magnetic field) drives the plasma rotation in the electron diamagnetic drift direction. The typical rotation velocity is 1.5 km/s at around ρ=0.65. During the MHD activity, the space potential changes slowly as shown in Fig. 3.9. However, the change of the space potential is less than 40 volts in each radial position, and no significant change of radial electric field is observed. It is suggesting that the $E_r \times B_\phi$ rotation velocity changes little during the one burst period.

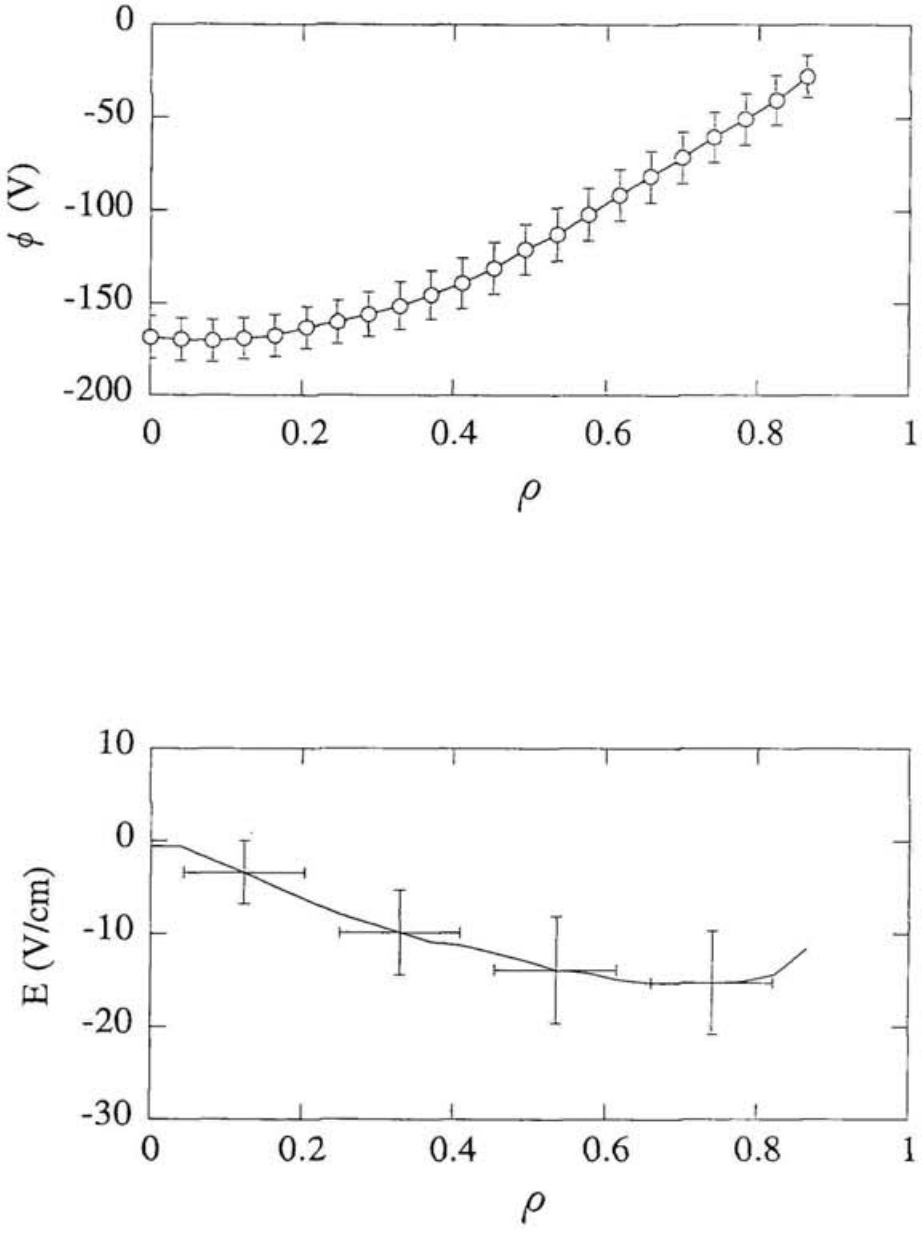

Fig. 3.8: (a) Typical electric potential and (b) radial electric field profiles in a neutral beam injected plasma (The electric field is determined by the potential profile).

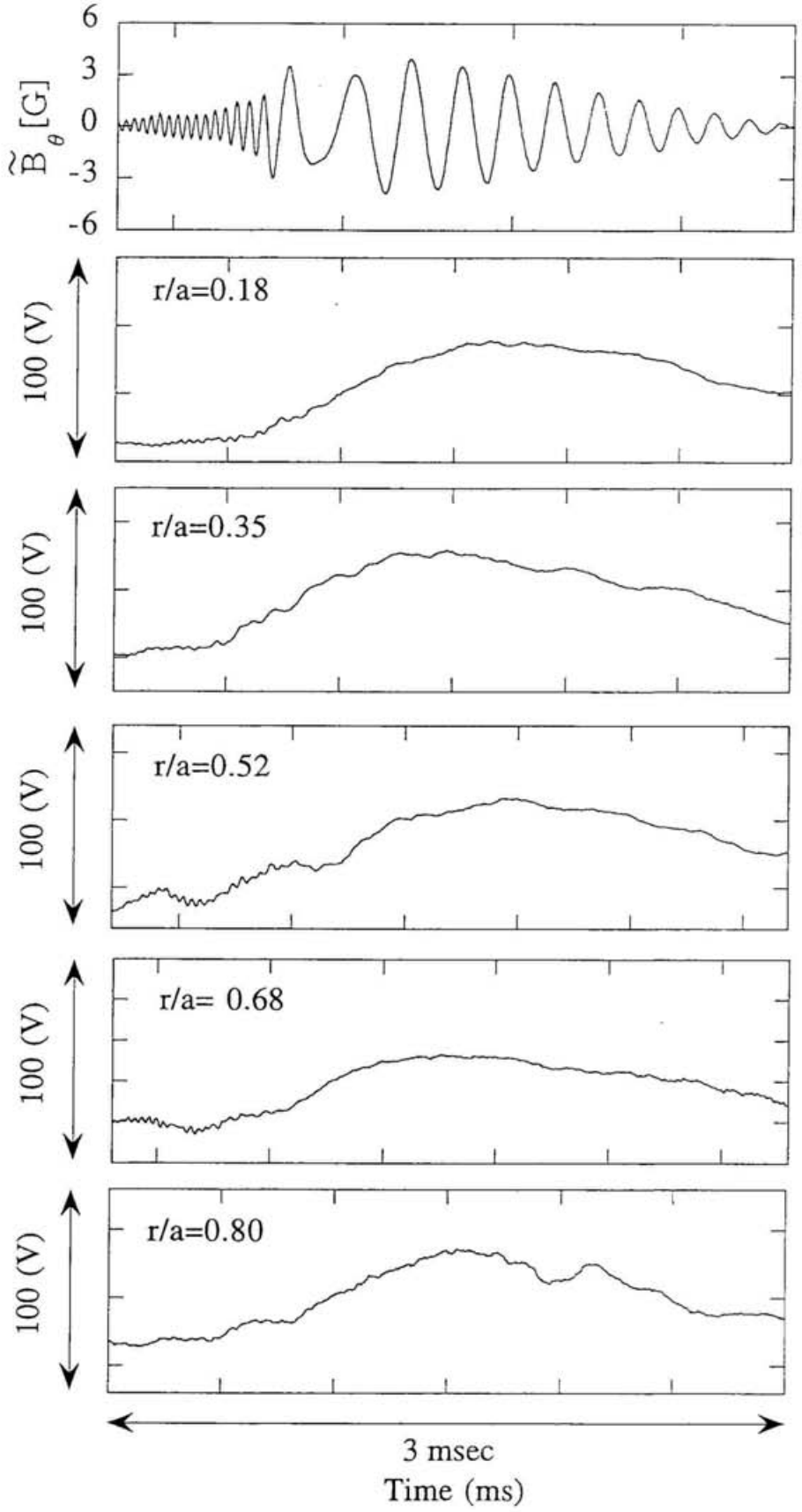

Fig. 3.9: Time variation of the electric potential during one burst period at different radial positons.

Chapter 4

Data analysis

4.1 Overview

Local and direct probing of plasma interior is considered to be a major advantage of HIBP diagnostic. However, beams passing through the plasma suffer various effects from plasma itself. For example, the probing beam attenuates as it penetrates into the plasma and thus suffers intensity modulation, which causes the contamination of the detected signals having local information. It is called path integral effect. Plasma potential measurement is generally considered not to be influenced by the path integral effect because of its diagnostic principle. However, in the presence of MHD fluctuations, beam acceleration (or deceleration) may occur due to the magnetic field fluctuation and may change the beam energy. Beam deflection causes an error in determining the beam energy with the energy analyzer. Such effects must be examined in detail.

In this chapter, analysis on the observed MHD fluctuations is described by emphasizing the effect of magnetic perturbation in determining the secondary beam energy and the plasma potential.

4.2 Path integral effect on potential fluctuation measurements

4.2.1 Introduction

The probing beam passing through the plasma gains energy due to acceleration (or deceleration) by the electric field along the beam trajectory. It is expressed as follows:

$$\begin{aligned}\delta W &= \int_a^b q\mathbf{E}\cdot d\mathbf{L} \\ &= \int_a^b q\left(-\nabla\phi - \frac{\partial \mathbf{A}}{\partial t}\right)\cdot d\mathbf{L} \\ &= q[\phi(a) - \phi(b)] - q\int_a^b \frac{\partial \mathbf{A}}{\partial t}\cdot d\mathbf{L} \quad ,\end{aligned} \tag{4.1}$$

where ϕ is the scalar potential, **A** is the vector potential, a and b are initial and final positions of the beam. If we take a at the position of the ion gun, b of the energy analyzer and s at the ionization position in the plasma, Eq (4.1) can be written as

$$\delta W = q\phi(s) - q\int_a^s \frac{\partial \mathbf{A}}{\partial t}\cdot d\mathbf{L} - 2q\int_s^b \frac{\partial \mathbf{A}}{\partial t}\cdot d\mathbf{L} \quad . \tag{4.1'}$$

When the magnetic oscillations are small, the pass integral term is negligible, and HIBP can measure the local plasma potential. In the presence of strong magnetic oscillations, however, it is necessary to examine this term. Actually fluctuations of **A** associated with low-m tearing modes have been observed as a toroidal displacement of the secondary beam at the detector position in the TEXT tokamak [45,46].

In tokamaks, beam trajectories are basically in the poloidal plane and the fluctuating part of the vector potential is dominated by the toroidal component. Then the path integral term is negligible. Unfortunately in HIBP for helical devices, the beam travels a certain distance in the toroidal direction and the path integral term should not necessarily be neglected.

In order to calculate the path integral term, it is necessary to know the detailed spatial structure of the vector potential, both on inside and outside of the plasma. It is not easy to measure it directly by HIBP in the real CHS configuration because of its non-axis-symmetry of the torus. In this thesis, a model vector potential for a cylindrical plasma column is assumed through theoretical and experimental approaches. Firstly, a simple spatial structure of the vector potential in the plasma is assumed based on an interchange mode theory and the contribution of the path integral term is evaluated for it. Here we take a fixed boundary plasma model and the vector potential outside the plasma is neglected (subsection 4.2.2). Next we will estimate the vector potential outside the plasma from the magnetic probe data. Since we do not have information on the vector potential inside the plasma, we assume the amplitude to be constant which can be connected to the curve for outside the plasma. We consider that this estimation will give us the upper limit of the contribution of path integral term (subsection 4.2.3). Then on the basis of these model calculation and experimental results of the spatial profile of the normalized T-B difference signal, we will estimate the path integral term inside the plasma more realistically (subsection 4.2.4).

4.2.2 Vector potential model -1 (theoretical approach)

In the reduced MHD equations for the heliotron/torsatron, the Ohm's law along the field line is expressed as [47]

$$\frac{\partial \Psi}{\partial t} = - \frac{\partial \Phi}{\partial \zeta} - \iota \frac{\partial \Phi}{\partial \theta} + \frac{J_\zeta}{S} \quad , \qquad (4.2)$$

where Ψ, Φ and ι are the total poloidal flux, perturbed potential and rotational transform, ζ and θ are toroidal and poloidal angle variables, respectively. The parameter S is the magnetic Reynolds number and J_ζ is the perturbed longitudinal current. The total poloidal flux is related with the ζ component of the vector potential as

$$\Psi = R_0 A_\zeta + \Psi_{vacuum} \quad , \qquad (4.3)$$

where R_0 and Ψ_{vacuum} are the major radius and the constant vacuum flux function. The magnetic Reynolds number S is about 10^6 in this experiment. We assume for simplicity that the third term in the right hand side of Eq. 4.2 is negligible. The perturbed potential can be expanded as

$$\tilde{\Psi} = \sum_{m=-\infty}^{\infty} \tilde{\Psi}_{mn}(\rho) \cos(m\theta - n\zeta) \qquad (4.4)$$

$$\tilde{\Phi} = \sum_{m=-\infty}^{\infty} \tilde{\Phi}_{mn}(\rho) \sin(m\theta - n\zeta) \quad .$$

Since we are considering the m/n=2/1 mode fluctuation, Eq. 4.2 is written as

$$\frac{\partial \tilde{\Psi}_{2/1}}{\partial t} = (1 - 2\iota)\,\tilde{\Phi}_{2/1} \quad . \tag{4.5}$$

Then the vector potential $A_\zeta / \partial t$ for m/n=2/1 mode is related with the perturbed potential $\tilde{\Phi}_{2/1}$ as

$$\frac{\partial \tilde{A}_\zeta}{\partial t} = \frac{1}{R_0}(1 - 2\iota)(\sin 2\theta)\,\tilde{\Phi}_{2/1} \quad . \tag{4.6}$$

Here we neglect the ζ dependence because of the long wave length compared with the beam travel distance.

Here we assume a simple potential profile as shown in Fig. 4.1, which has long correlation length and has a single peak (normalized to unity) at the q=2 rational surface and vanishes at the plasma center and edge. The rotational transform profile with the volume averaged beta value of 0.2% (Fig. 1.4) is used [48]. The vector potential profile calculated in this model is shown in Fig. 4.2.

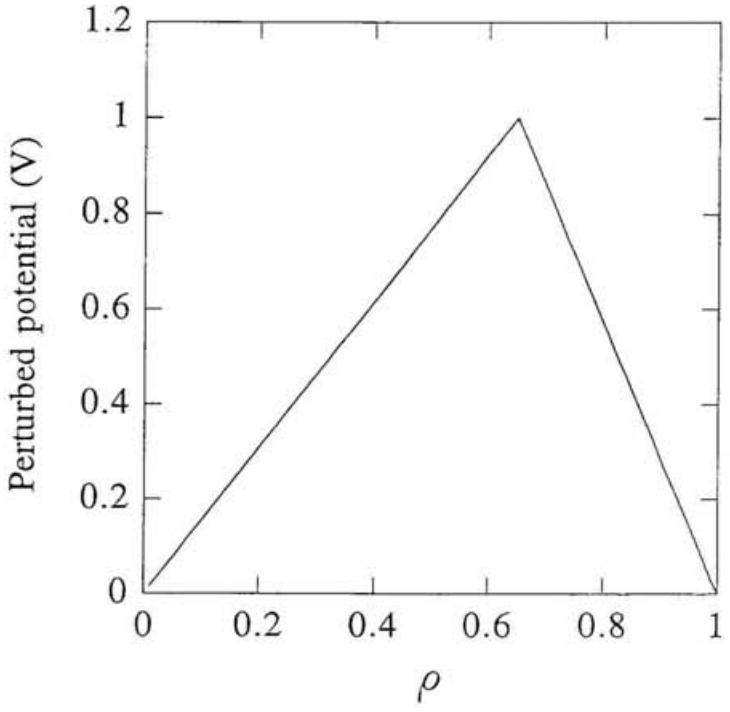

Figure 4.1: Model potential profile (maximum value is normalized to unity).

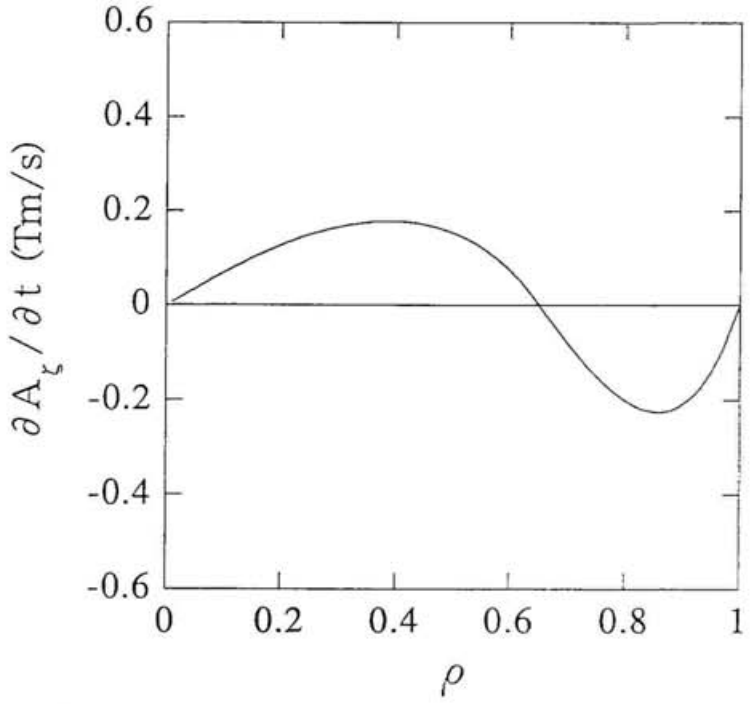

Figure 4.2: Time derivative of the vector potential calculated from the model potential profile in Fig. 4.1.

Then the path integral term can be calculated as follows:

$$\delta W = \sum_{i=1,2} q_i \int \frac{\partial \tilde{A}}{\partial t} \zeta(\rho,\theta) \cdot dl_{\zeta,i}(\rho,\theta)$$

$$= \frac{1}{R_0} \sum_{i=1,2} q_i \int (1 - 2\epsilon(\rho)) \{-\cos(2\theta + \delta)\} \tilde{\Phi}_{2/1}(\rho) \cdot dl_{\zeta,i}(\rho,\theta) , \quad (4.7)$$

where dl_ζ is the ζ component of the primary and secondary beam path length which have been calculated by beam trajectories and is a function of ρ and θ. In Eq. 4.7, θ dependence is taken as $\{-\cos(2\theta + \delta)\}$ just for convenience of calculation, where δ represents the phase relation between the beam line and the poloidal mode structure of the instability. Figure 4.3 shows the calculated energy gain as a function of beam location for the sample position of ρ=0.6 and δ=0. The total energy changes due to the path integral effect is less than 0.03 V. Summary of the calculation for each sample position as a function of δ is shown in Fig. 4.4 , which shows the ratio of vector potential term to scalar potential term. The ratio varies with the phase δ , but within several percent.

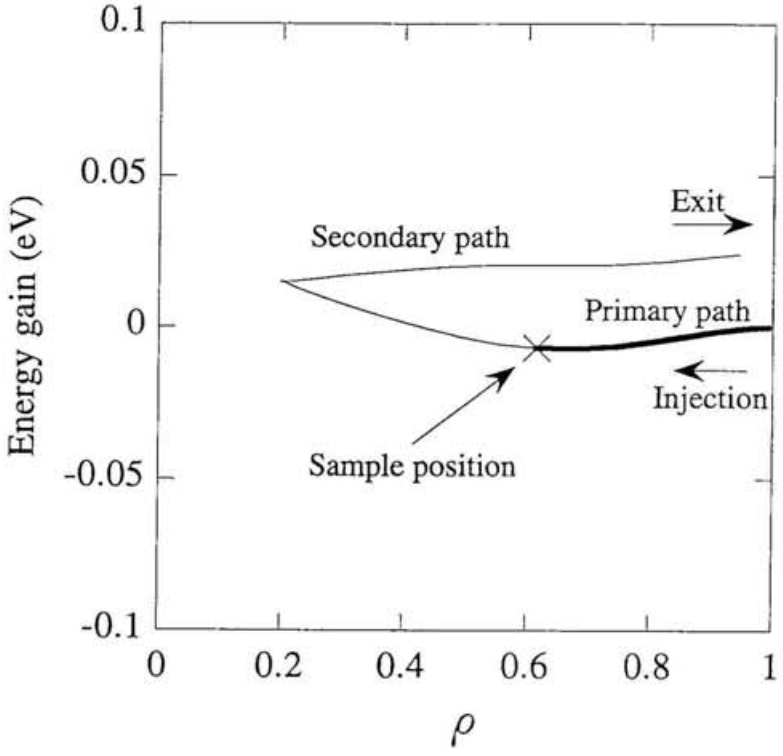

Figure 4.3: Energy gain due to the path effect for each radial position.

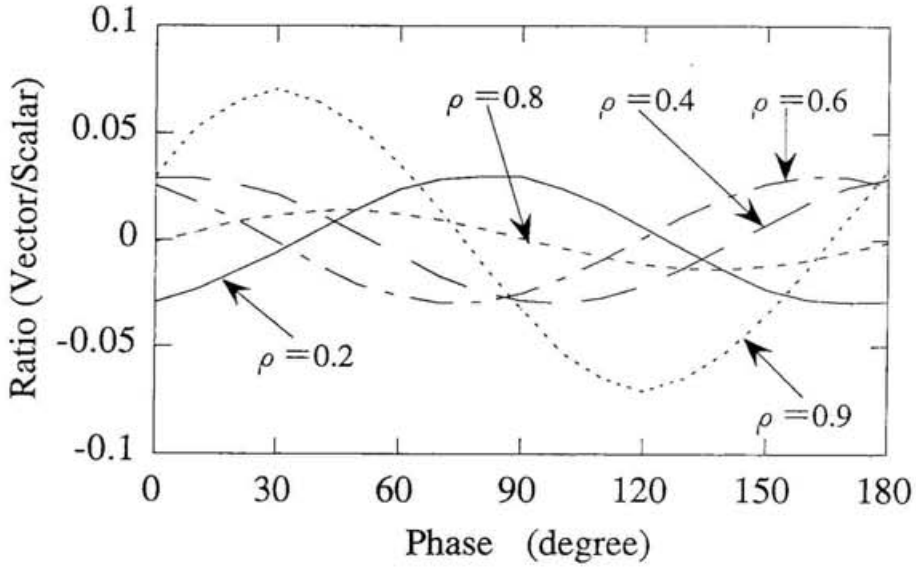

Figure 4.4: The ratio of maximum values of vector potential and scalar potential terms for several sample positions.
The horizontal coordinate presents the phase relation between the beam trajectory and the poloidal mode structure.

4.2.3 Vector potential model-2 (with magnetic probe data)

The previous calculation shows the path effect due to the vector potential term is small. However this is a restricted case because the radial eigen function has an odd structure near q=2 surface and the path integral cancels the local effect. In this subsection, we will estimate the path effect assuming radially uniform A_ζ profile, where cancellation of local effect does not occur. In order to estimate the A_ζ value at the plasma edge, we will estimate the vector potential outside the plasma from the magnetic probe data. In a cylindrical coordinate, the vector potential A_ζ(outside the plasma) satisfies the Laplace's equation

$$[\nabla \times (\nabla \times A_\zeta)] = \frac{\partial^2 A_\zeta}{\partial r^2} + \frac{1}{r}\frac{\partial A_\zeta}{\partial r} - \frac{\partial^2 A_\zeta}{\partial \theta^2} + \frac{\partial^2 A_\zeta}{\partial \zeta^2} = 0 \quad (4.7)$$

If the perturbation of A_ζ is expanded as

$$A_\zeta = \sum_{m=-\infty}^{\infty} A_{\zeta m,n}(r)\cos(m\theta - n\zeta) \quad . \quad (4.8)$$

Eq. (4.7) is expressed as the following differential equation for the mode number m:

$$\frac{\partial^2 A_{\zeta,m}}{\partial r^2} + \frac{1}{r}\frac{\partial A_{\zeta,m}}{\partial r} - \frac{m^2}{r^2}A_{\zeta,m} = 0 \quad , \quad (4.9)$$

where we neglect the ζ dependence of instabilities in HIBP observation area ($\delta\ \zeta \sim 22.5^{\circ}$). For $m \neq 0$, the solution is written as

$$A_{\zeta,m}(r) = C\ r^{m} + D\ r^{-m}, \qquad (4.10)$$

where C and D are integral constants. Then it is reasonable to relate $A_{\zeta,m}$ at the plasma edge a with $A_{\zeta,m}$ at the magnetic coil position r_c as

$$A_{\zeta,m}(a) = \left(\frac{r_c}{a}\right)^{m} A_{\zeta,m}(r_c). \qquad (4.11)$$

In the cylindrical coordinate, the magnetic fluctuation $\tilde{B}_{\theta}$ is represented as

$$\tilde{B}_{\theta,m}(r_c) = -\frac{\partial \tilde{A}_{\zeta,m}(r_c)}{\partial r}, \qquad (4.12)$$

with assuming $\partial A_r / \partial \zeta = 0$. Substituting Eq. 4.11 into Eq. 4.12, the time derivative of perturbed vector potential at the plasma edge can be derived as

$$\frac{\partial \tilde{A}_{\zeta,m}(a)}{\partial t} = \frac{r_c}{m}\left(\frac{r_c}{a}\right)^{m} \frac{\partial \tilde{B}_{\theta,m}(r_c)}{\partial t}. \qquad (4.13)$$

The amplitude of $\partial \tilde{B}_\theta / \partial t$ at r_c is obtained from the magnetic probe data (Fig. 4.5). Figure 4.6 shows the model vector potential profile used here. In order to estimate the maximum value of vector potentail term, we have extended the Eq. 4.13 into plasma interior up to q=2 surface (ρ =0.65). Inside of this surface, a uniform A_ζ is assumed. Path integral term in Eq. 4.1' is calculated as

$$\delta W = - q_1 \int_a^s \frac{\partial \tilde{A}}{\partial t} \cdot dl_1 - q_2 \int_s^b \frac{\partial \tilde{A}}{\partial t} \cdot dl_2 \quad . \qquad (4.14)$$

As is shown in Fig. 4.7, the path integral term with this model is less than a few volt for each sample position. Contributions from plasma outside is less than 10 % of the total path effect for this model vector potential.

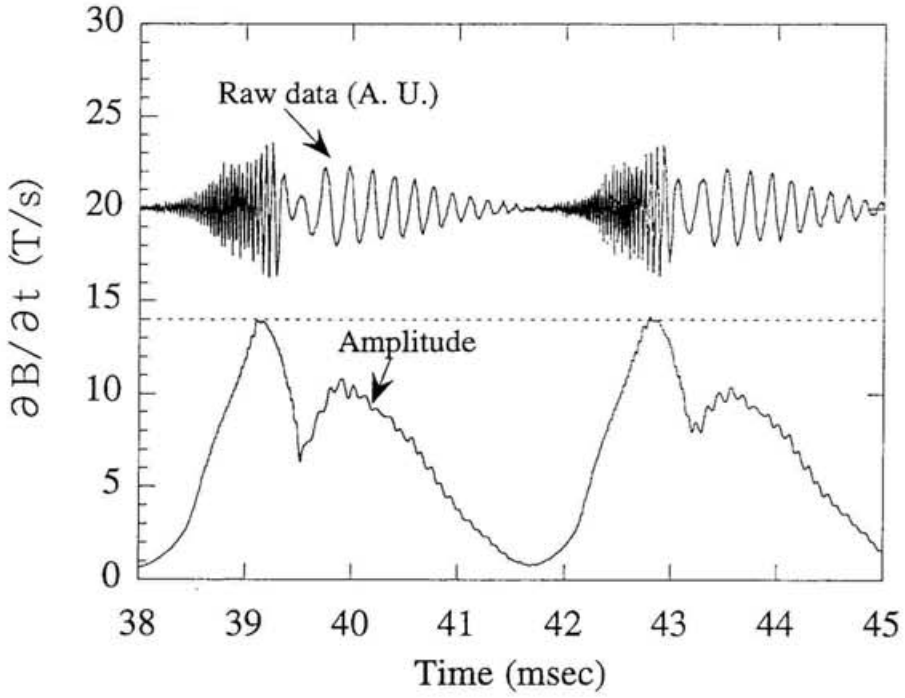

Figure 4.5: Time derivative of magnetic fluctuations with a Mirnov coil (upper trace), and its amplitude (lower trace).

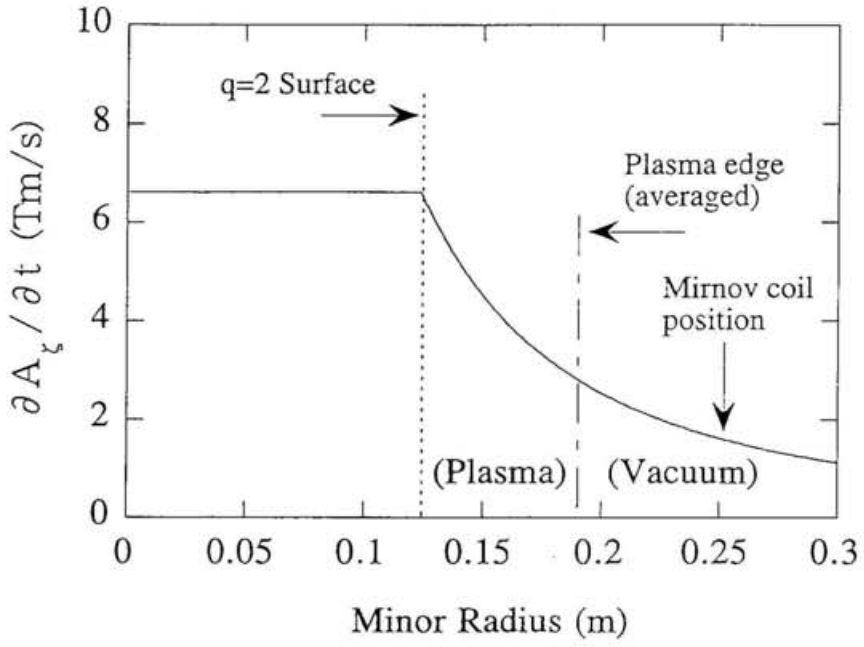

Figure 4.6: Model vector potential profile-2.
The curve for plasma outside is estimated from the magnetic probe data.

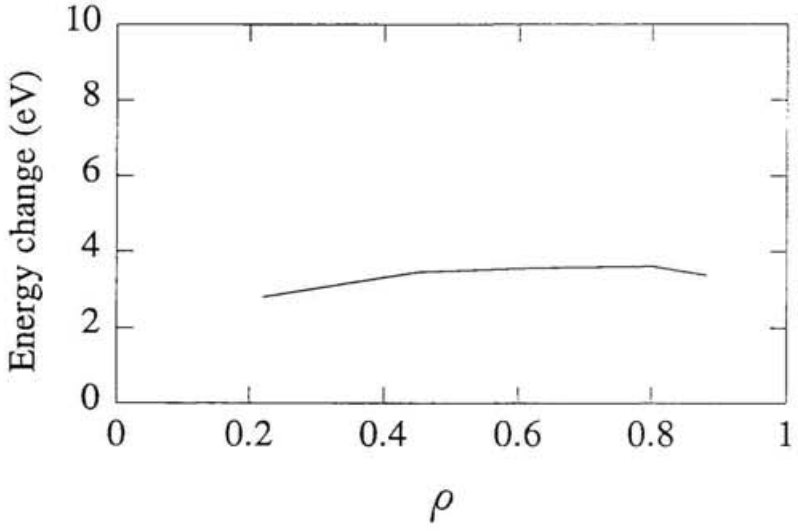

Figure 4.7: Path integral effect due to the model vector potential shown in Fig. 4.6

4.2.4 Vector potential model-3 (with HIBP data)

As is shown in the previous two subsections, contribution of the path integral effect due to the model vector potential to the real potential fluctuations is small. In this subsection, the path integral term is calculated in accordance with the HIBP data. Since the burst-type mode changes its frequency and amplitude during the burst period, the path integrated value depends on time. Here we calculate it at its maximum. By assuming that the normalized T-B difference shown in Fig. 3.6 (b) represents the scalar potential, the time derivative of the vector potential can be obtained from Eq. 4.6 (Fig. 4.8). Resulting path integral effects are obtained for each radial position as shown in Fig. 4.9. Here we assumed again a fixed boundary plasma column. It is confirmed that the path integral effect due to the fluctuating vector potential is negligible for the observed MHD instabilities in CHS.

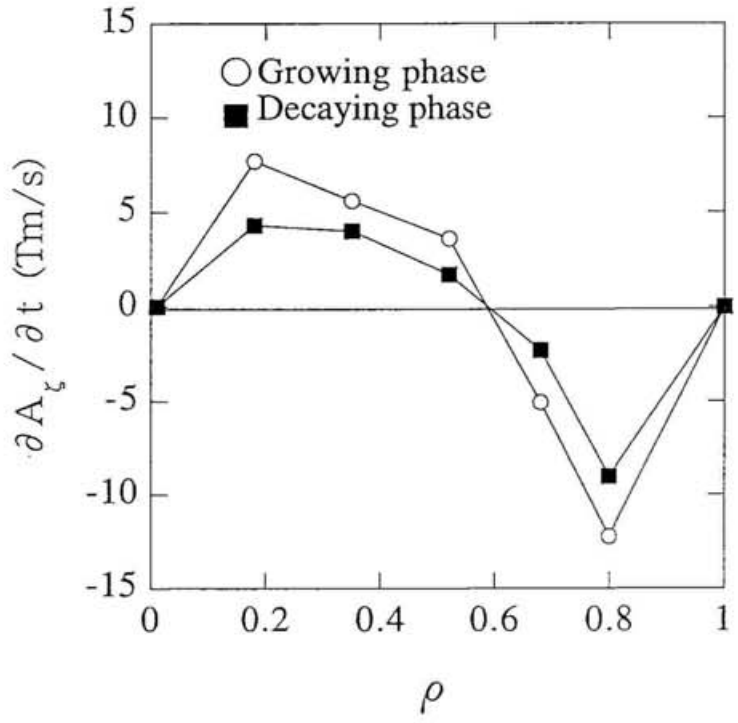

Figure 4.8: Time derivative of the vector potential
on the assumption of scalar potential shown in Fig. 3.6 (b).

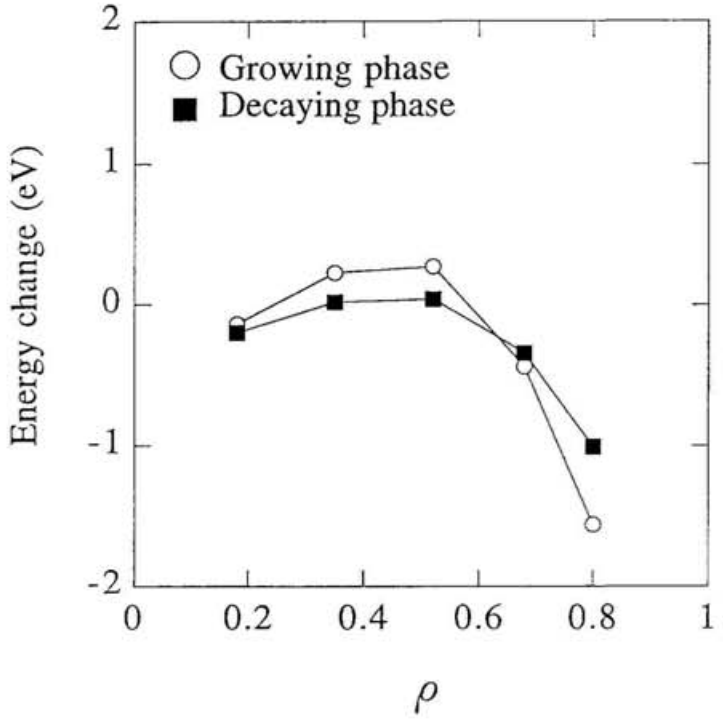

Figure 4.9: Path integral effect due to fluctuating vector potential as shown in Fig. 4.8.

4.3 Errors in energy analyzer

The analyzer is located at a certain distance so as to avoid the effect of the stray magnetic field. In this situation, the measured potential ϕ has the following relation with the true plasma potential ϕ_0,:

$$\phi = \phi_0 + \delta\phi_1 + \delta\phi_2(\delta\theta, \delta\alpha) \quad . \qquad (4.15)$$

Where, $\delta\ \phi_1$ is an offset due to the unbalance between accelerator and analyzer voltages, and $\delta\ \phi_2$ is a correction term due to a small deviation of the beam injection angle into the analyzer. The angles $\delta\ \theta$ and $\delta\ \alpha$ represent the deviation of the vertical and horizontal beam injection angle from the ideal value of 30° and 0°, respectively. By the calibration procedure with the gas ionization method, $\delta\ \phi_1$ can be determined as a constant value. In the presence of MHD oscillations, the angle $\delta\ \theta$ and $\delta\ \alpha$ possibly fluctuate due to the beam deflection by the fluctuating magnetic field, and the third term in Eq. (4.15) should be examined precisely. The potential variation from the vertical injection angle $\delta\ \theta$ is shown in Fig. 4.10. Owing to the second order focusing property of the energy analyzer, uncertainty of the potential measurement due to $\delta\ \theta$ is less than a few volts in the present experimental conditions ($\delta\ \theta < 0.5^\circ$). However, since the analyzer has only the first order focusing in the α direction, $\delta\ \phi_2$ is sensitive to $\delta\ \alpha$ and is approximated as follows:

$$\delta\phi_2 = \left(1 - \frac{1}{\cos^2\alpha}\right) q_s V_A G(\theta_I, \alpha) \quad , \qquad (4.16)$$

where q_s and V_A are the charge of secondary ions and the analyzer voltage, respectively, and $G(\theta_I, \alpha)$ is the gain of the analyzer. The $\delta\alpha$ is determined by the following relation:

$$\delta\alpha \equiv \delta\tilde{\alpha} + \delta\bar{\alpha}$$

$$\delta\tilde{\alpha} < \tan^{-1}\left(\frac{\delta y_1 + \delta y_2}{L}\right) \qquad (4.17)$$

$$\delta\bar{\alpha} = \tan^{-1}\left(\frac{\delta y_3}{L}\right) \quad ,$$

where δy_1 and δy_2 are the fluctuating toroidal displacements of the secondary beam in the plasma and at the detector position, respectively, δy_3 is the averaged toroidal beam displacement at the detector position, and L is the path length of the secondary beam. The maximum value of δy_1 is calculated with the magnetic field perturbation in the plasma which is estimated from the magnetic probe data. On the other hand, δy_2 and δy_3 are determined by the left-right balance of the detected signals (Fig.4.11 (a)). Using those values of $\delta y_1 < 3$ (mm) and $\delta y_2 < 4$ (mm) , it is found that $\delta\tilde{\alpha} < 0.15^\circ$. As a result, the uncertainty of beam energy due to beam deflection by the MHD fluctuations is estimated for each observation point (Fig.4.11 (b)).

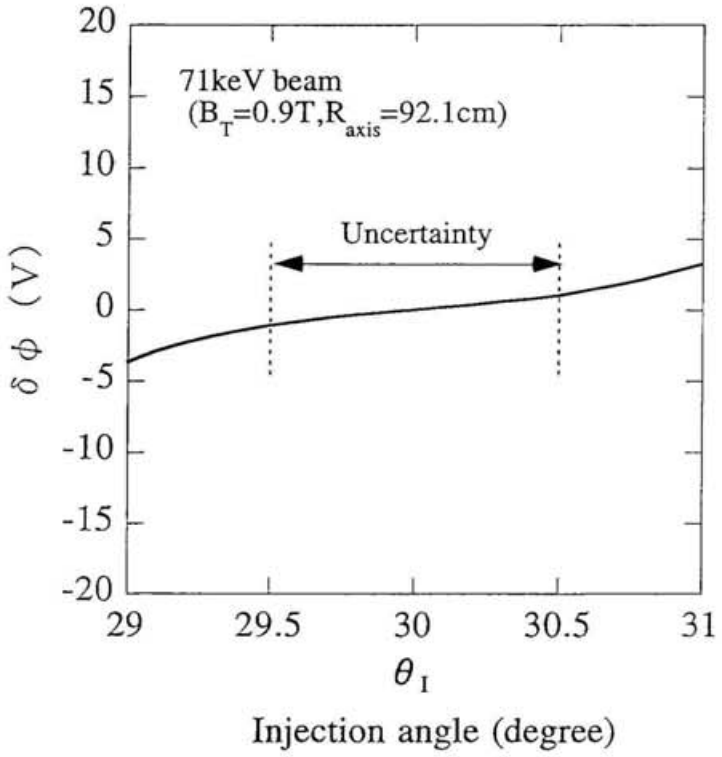

Figure 4.10: Error in the determination of beam energy
due to the uncertainty from vertical injection angle (Gain curve).

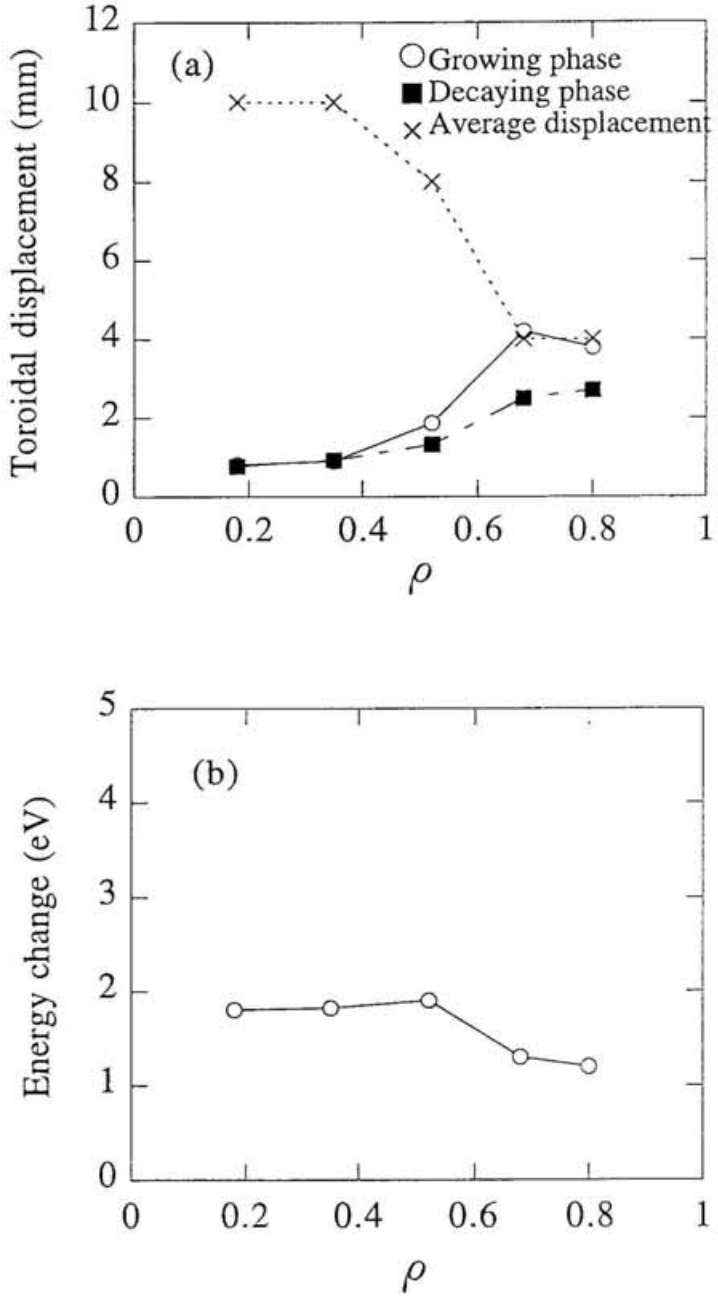

Figure 4.11: (a) Toroidal displacement of the secondary beam on SPD and its fluctuations for each sample position.
(b) Resultant error in determining beam energy.

4.4 Radial fluctuation profiles and correlation analysis

Figure 4.12 shows the spatial variation of the amplitude of potential fluctuation for growing and decaying phases. The error bars are determined by the discussions in the previous two subsections. The fluctuation level is high at around ρ=0.5~0.7, where the q=2 rational surface is located. It is also shown that the potential fluctuation is small all over the plasma radii in the decaying phase. Since the noise level of the detector corresponds to several volts, potential fluctuations in the central region are considered to be small.

In order to discuss the detailed internal structure of MHD oscillations, the density fluctuation profile as well as the potential fluctuation profile is necessary. Figure 3.7(b) shows the spatial variation of the sum signal fluctuations. The fluctuation level is higher outside the q=2 surface during the whole burst period. However, because of strong path effect due to beam attenuation in the plasma interior, it is not a true density fluctuation profile especially in the core region. In the case of micro-turbulence in tokamak experiments like TEXT and JIPPT-IIU, path integral effect on the local fluctuation measurement has been discussed in detail. However, for MHD oscillations where radial correlation length is large, no practical method of reconstruction of the local density fluctuation profile has been developed. It will be discussed elsewhere [49]. It is difficult, at the monent, to discuss the correlation between local density and potential fluctuations precisely.

In this thesis, we discuss the global characteristic of the MHD oscillation from the correlation analysis between the magnetic field fluctuation obtained from one of the Mirnov coils and the potential fluctuation from HIBP. The procedures for the correlation analysis are as follows. For two detected signals X(t) and Y(t), the autopower and crosspower spectrum P_1 (f), P_2 (f) and P_{12}(f) are calculated as:

$$\begin{aligned} P_1(f) &= E\left[\frac{2\pi\langle X(f)\,X^*(f)\rangle}{T}\right] \\ P_2(f) &= E\left[\frac{2\pi\langle Y(f)\,Y^*(f)\rangle}{T}\right] \\ P_{12}(f) &= E\left[\frac{2\pi\langle X(f)\,Y^*(f)\rangle}{T}\right] \end{aligned} \qquad (4.18)$$

Where T is the time window and E means the ensemble average, and X(t) , Y(t) are Fourier transform of the detected signals expressed as follows,

$$\begin{aligned} X(f) &= \frac{1}{2\pi}\int_{-\infty}^{\infty} X(t)\,\exp[-i2\pi ft]\,dt \\ Y(f) &= \frac{1}{2\pi}\int_{-\infty}^{\infty} Y(t)\,\exp[-i2\pi ft]\,dt \end{aligned} \qquad (4.19)$$

The coherence between the two signals is calculated as:

$$Coh(f) = \left(\frac{K_{xy}^2(f)+Q_{xy}^2(f)}{P_1(f)\,P_2(f)}\right)^{1/2}, \qquad (4.20)$$

where, $K_{xy}(f)$ and $Q_{xy}(f)$ are the real and the imaginary parts of the crosspower spectrum, respectively. The phase between the two signals is expressed as:

$$\theta_{xy}(f) = \tan^{-1}\left(\frac{Q_{xy}(f)}{K_{xy}(f)}\right) \quad . \qquad (4.21)$$

The sampling time of magnetic probe is 4 μs (HIBP is 2 μs), and the limit of frequency range is 125 kHz (Nyquist frequency $f_N=1/2\,\tau$, τ :sampling time). Since the time period of the observation for each sample positions is 18 ms and the ensemble average is taken by 10 subwindows, the frequency resolution of the present analysis is about 1 kHz.

Figure 4.13 shows the auto power spectrum, coherence and phase relation of the magnetic fluctuation detected by the No.10 magnetic probe in the poloidal array and the potential fluctuation. The correlation is stronger in the frequency range between 15 to 25 kHz which corresponds to the growing phase while it is weak in the low frequency region around 5 kHz which corresponds to the decaying phase. It is also shown that the phase difference change almost $\pi/2$ during the growing phase, which suggests the nonlinear evolution of MHD instabilities, although the phase relation between the local density fluctuation and the potential fluctuation is not known from these analyses.

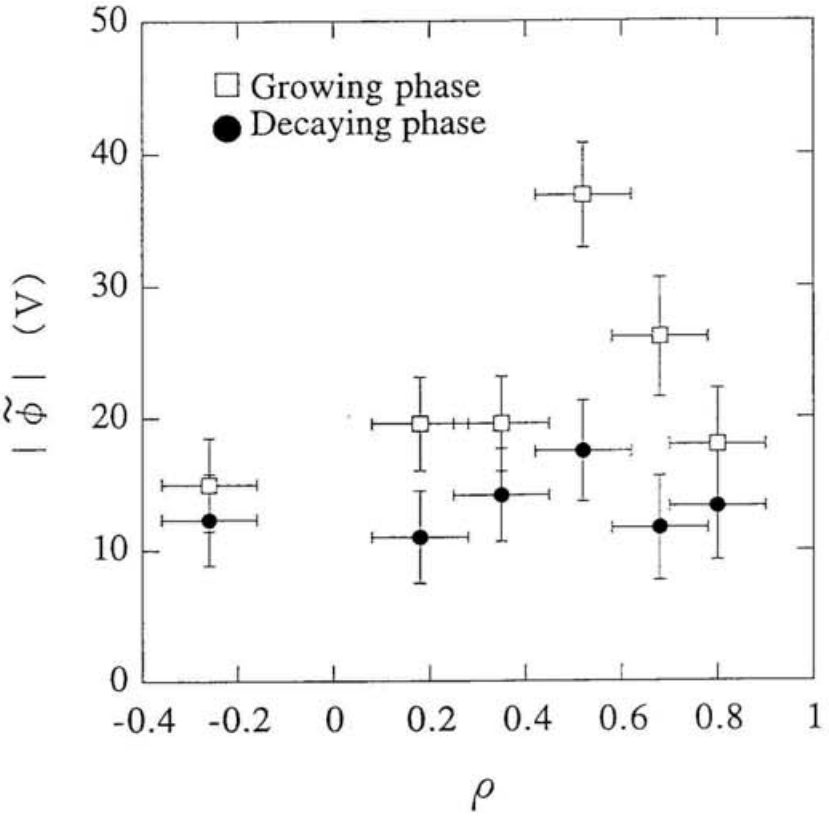

Figure 4.12: Amplitudes of potential fluctuations
for several observation points (r/a means normalized minor radius).

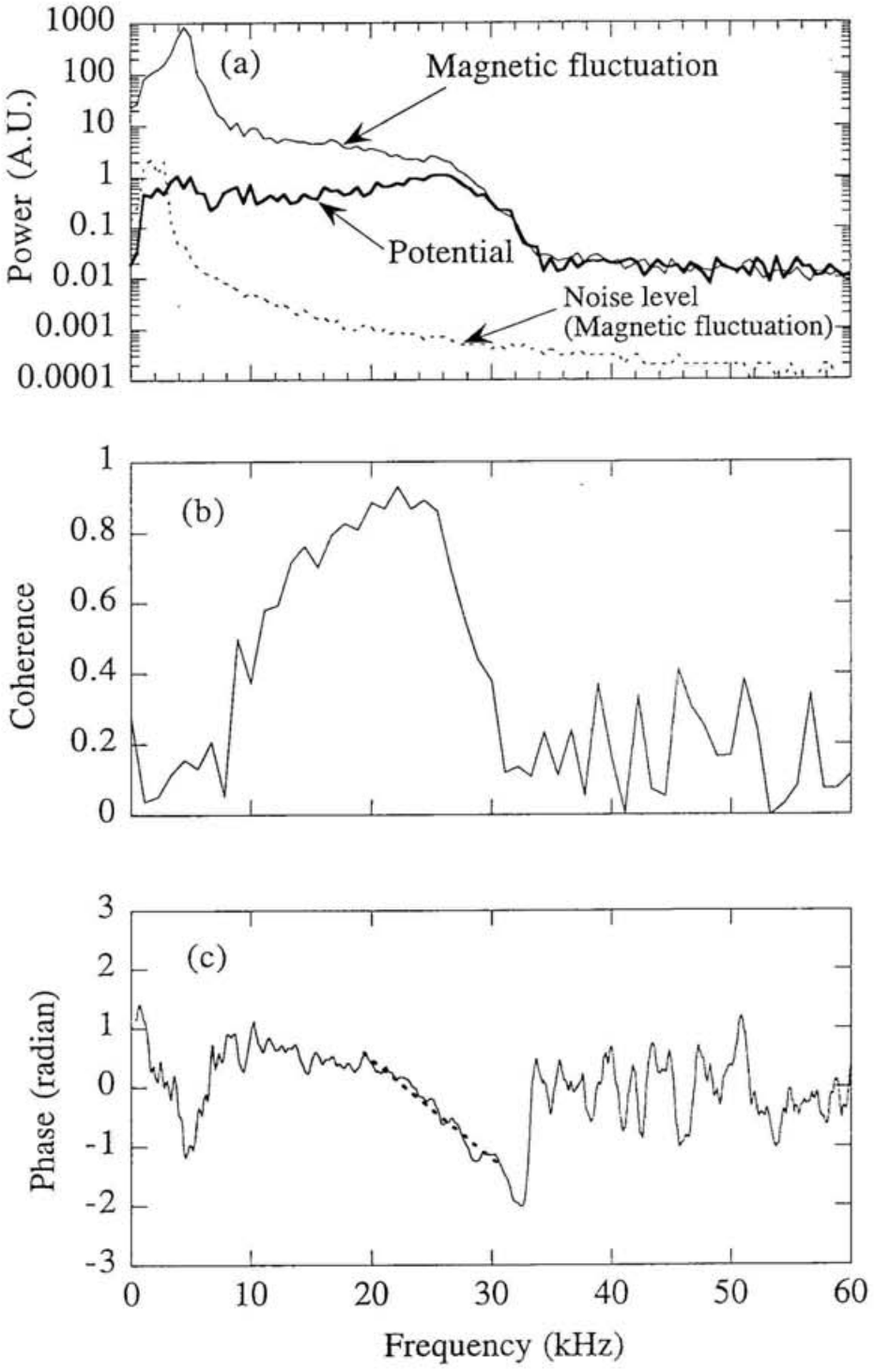

Figure 4.13: Power spectrum, coherence and phase relation between magnetic and potential fluctuations. (ρ ~0.4)

Chapter 5

Discussion

5.1 Path integral effects during MHD activities

It is shown that the path integral effect on the potential fluctuation measurement is negligible for the observed burst type MHD oscillation. Since the path effect is dominated in the plasma region and depends on the mode structure and amplitude, vector potential model is important for such calculation. The present analysis is based on rather simple models with the fixed plasma boundary. Fortunately in the case of m/n=2/1 mode, the radial eigen function of the vector potential has an odd structure, and the path effect is reduced because of cancellation due to integration along the total beam path, which is not always true. It is also noted that the toroidal geometry is not included, because the cylindrical plasma model is appropriate for the purpose of the present analysis. In a tokamak, which is an axisymmetric torus, the vector potential has been directly obtained from the L-R difference because of the toroidal momentum conservation. However, in a helical device, there is no toroidal symmetry and the L-R difference is not directly connected with the vector potential. Simulation will be necessary for more accurate estimation.

In the above analysis, the toroidal component of vector potential has been examined. The effect from the radial or azimuthal component is not discussed. Because a low mode number MHD instability is associated with a perturbed current

along the field line, which mainly contribute to the toroidal component of the perturbed vector potential, the other components are considered to be small. Even if these components are comparable to the toroidal component, the total path effect is still small in the present burst type MHD oscillation. In general, it is necessary to confirm the vector potential dependence on each MHD mode structure.

On the other hand, the path integral effect on the density fluctuation measurement is more serious than on the potential fluctuation measurement. The secondary beam current (the sum signal) from the sample volume $\mathbf{r}_{sv}$ is expressed as

$$I_s(\mathbf{r}_{sv}) = 2I_0\ \sigma_{12}(\mathbf{r}_{sv}) l_{sv}\, n_e(\mathbf{r}_{sv}) \exp\left(-\int_{r_{in}}^{r_{sv}} n_e(\mathbf{r}_{sv})\,\sigma_1\,dl\right) \times \exp\left(-\int_{r_{sv}}^{r_{ex}} n_e(\mathbf{r}_{sv})\,\sigma_2\,dl\right) \tag{5.1}$$

where, I_0 and l_{sv} are the primary beam current and the sample volume length, respectively, σ_1, σ_2 and σ_{12} are the effective total ionization cross sections for primary beam, secondary beam and the ionization cross section from primary to secondary beams, r_{in} and r_{ex} are the beam injection and exit positions of the plasma. Fluctuations in the sum signal include not only the local density fluctuations at the sample volume but also the effect of beam modulation due to density fluctuations along the primary and secondary beam trajectories. If $\int \tilde{n}\,\sigma\,dl \ll 1$, we can linearize eq. (5.1) by expanding the exponential term and obtain

$$\frac{\tilde{I}s}{Is} = \frac{\tilde{n}_e}{n_e} - \left(\int_{r_{in}}^{r_{sv}} \tilde{n}_e(r)\,\sigma_1\,dl + \int_{r_{sv}}^{r_{ex}} \tilde{n}_e(r)\,\sigma_2\,dl\right) . \tag{5.1'}$$

Reconstruction of local density fluctuation profile from the beam intensity fluctuation profile requires an iterative procedure. Such analysis has been discussed for micro-turbulence study in the TEXT tokamak, where the radial correlation length is small compared with the plasma radius[50-54]. In the case of fluctuations with a long correlation length like MHD instabilities, such process can not be directly applied [49]. In addition, more precise data points will be necessary in order that the reconstruction procedure should be accurate. It is left for a future work. If the reconstruction of density fluctuation profile is successful, then the local correlation analysis between density and potential fluctuations is possible which should improve understanding of internal structures of MHD modes.

5.2 Mode propagation

NBI heated plasma generally exhibits a negative space potential and thus the inward directed radial electric field. The resultant $E_r \times B_t$ drift (E_r: radial electric field, B_t: toroidal magnetic field) drives the plasma poloidal rotation in the electron diamagnetic direction. The poloidal propagation velocity of any fluctuation modes suffers from the Doppler effect due to this drift. Then the observed oscillation frequency will be modified as follows[55,56];

$$f_{obs} = f_{mode} - \left(\frac{k_\theta}{2\pi}\right)\left(\frac{E \times B}{B^2}\right) \quad , \qquad (5.2)$$

where f_{obs} and f_{mode} are the observed frequency and the fluctuation mode frequency, respectively. The poloidal wave number k_θ is determined with the average radius of the q=2 surface and the poloidal mode number m=2. The sign is defined so that the propagation in the ion diamagnetic drift has positive frequency. In our experiment, the static potential profile does not change much during MHD activities and the radial electric field is about 1.5 kV/m around the q=2 surface. The $E \times B$ drift frequency is about 5 kHz. Taking this term into account, we can estimate that the mode frequency is changing from 25 kHz to 15 kHz during the growing phase and 0 kHz in the decaying phase.

Next we compare these frequencies with the drift frequency, which is the characteristic frequency for pressure driven instabilities. Since we are considering MHD modes, the ion diamagnetic drift velocity is concerned.

It is calculated from the experimental observation on ion temperature and density profiles. The poloidal wave number can be estimated from the mode number m and the radius of rational surface r_s as $k_\theta = m/r_s$.

Figure 5.1 shows a typical ion temperature profile measured by a charge exchange spectroscopy in a similar shot. An electron density profile is obtained by Thomson scattering and the absolute value is calibrated by an HCN laser interferometer as shown in Figure 5.2. The pressure profile is determined from these data. By assuming the fitting curve as

$$P(\rho) = P_0 (1 - \rho^2)^{\alpha} \quad [kJ/m^3] \quad , \qquad (5.3)$$

those parameters of $P_0 \sim 1.2$ and $\alpha \sim 2.05$ are obtained, which is shown in Fig. 5.3(a). Then the ion diamagnetic drift velocity v_{dia} is obtained as shown in Fig. 5.3 (b). This value corresponds to the mode frequency about 10 kHz in the case of poloidal mode number m=2.

The result indicates that the observed mode propagation velocity is twice as large as the ion diamagnetic drift velocity in the growing phase. While in the decaying phase, the mode is fixed to the E×B plasma rotation.

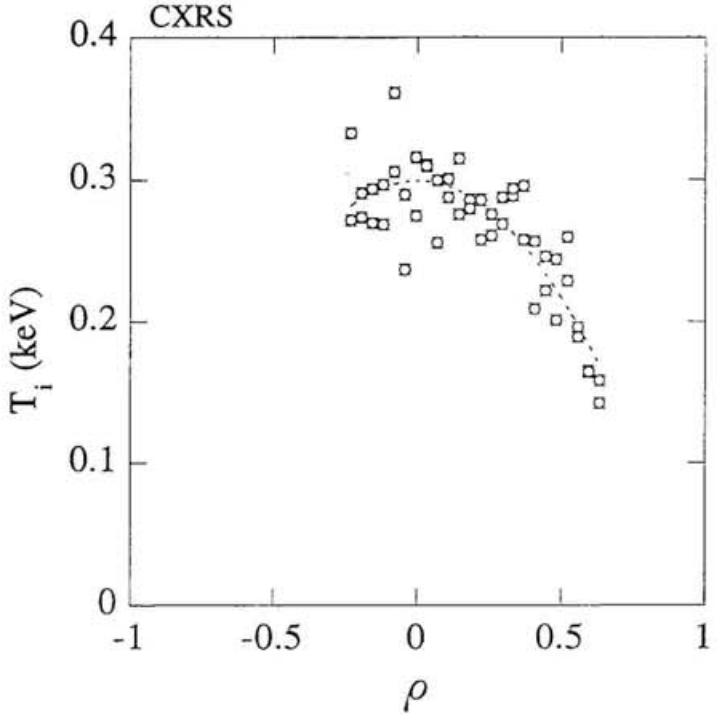

Figure 5.1: Ion temprature profile in a similar shot.
(charge exchange spectoroscopy)

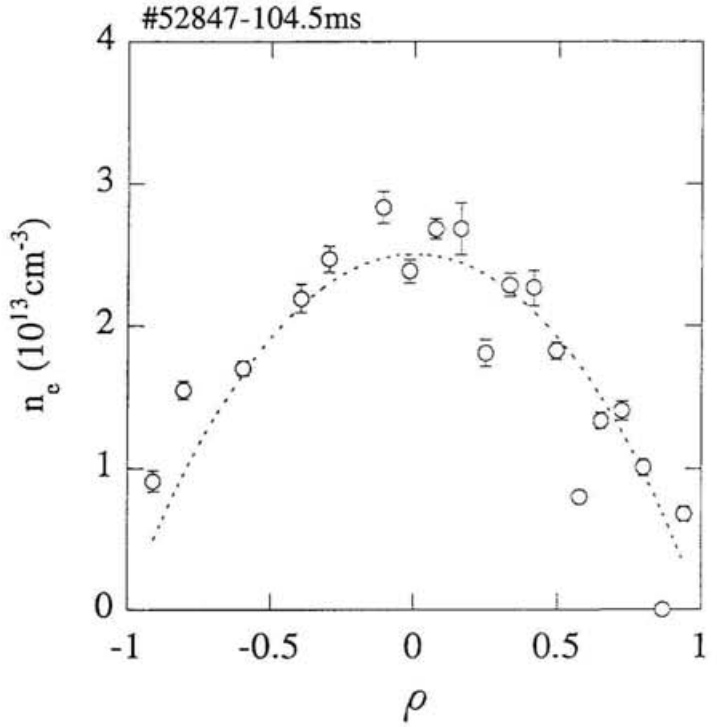

Figure 5.2: Electron density profile.
(Thomson scattering and HCN laser interferometer)

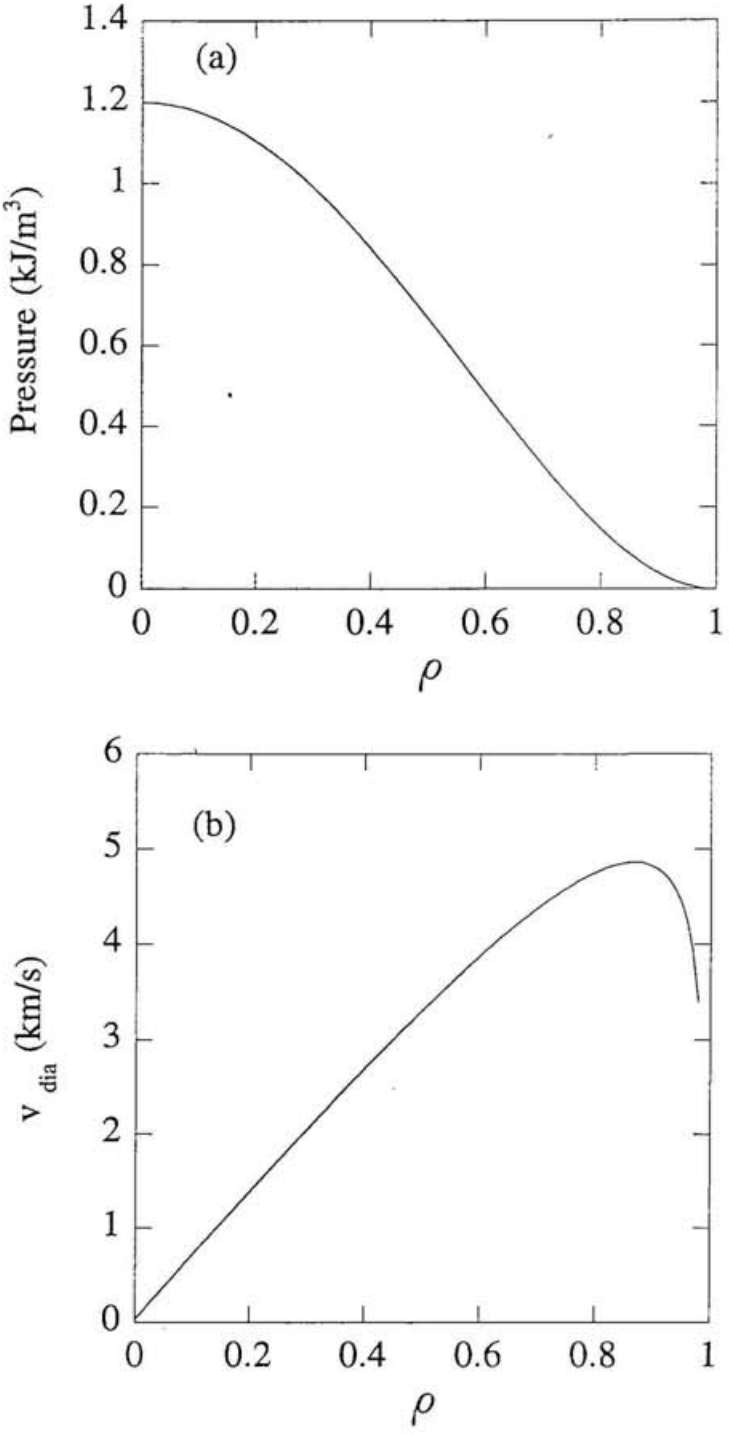

Figure 5.3: (a) Pressure profile and (b) ion diamagnetic drift velocity (n_i=n_e is assumed).

5.3 Comparison with interchange mode theory

In heliotron/torsatron configuration, the pressure driven interchange mode is most dangerous because of its magnetic hill configuration in the peripheral region, although it is expected to be stabilized by strong magnetic shear. In the case of NBI co-injection, the beam driven current is considered to be centrally peaked and increases the rotational transform near the center and then reduces the effect of shear stabilization at the peripheral.

First we shortly review the growing mechanism of the pressure driven interchange instability. As is shown in Fig. 5.4, density perturbation at a rational surface will induce charge separation due to their diamagnetic drifts of electrons and ions. The resultant electric field enhances the plasma displacement through $E_1 \times B_0$ motion, where $E_1 (= \nabla \phi)$ is the perturbed electric field in the poloidal direction. Then the instability grows.

The radial structure of the measured potential fluctuation which has a strong peak around the q=2 surface is basically consistent with this picture. Propagation velocity of the interchange mode is expected to be at the ion diamagnetic drift velocity. Difference between the observation and theoretical estimation is not understood. The continuous change of phase difference between magnetic fluctuation and potential fluctuation in the growing phase seems to be suggesting nonlinear evolution. It is considered that the large amplitude of instability can lead to pressure flattening and decreasing of diamagnetic drift velocity as observed in the experiment[57,58].

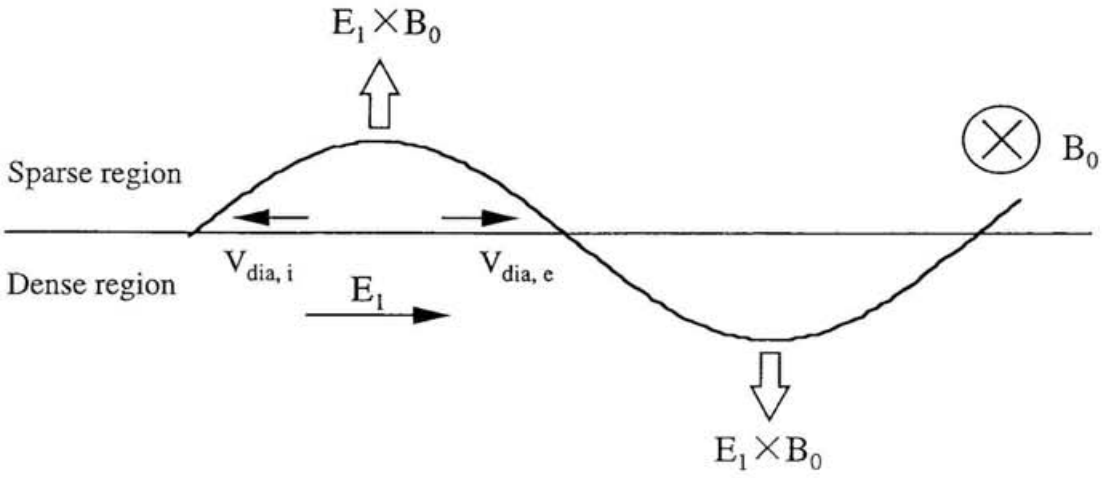

Figure 5.4: Schematic view of development of plasma displacement in pressure driven interchangemode.

Since the present burst mode (second type) appears when the beam driven current is rather large (~7 kA), reduction of magnetic shear seems to contribute to the mode excitation[59]. All those characteristics are qualitatively consistent with the pressure driven interchange theory.

On the other hand, the mode structure in the decaying phase is completely different. The magnetic fluctuation is larger than that in the growing phase, while the potential fluctuation is suppressed. The suppression of potential fluctuation is all over the plasma radii. The mode is fixed to the plasma rotation. These results can be interpreted by a m=2 island formation at the q=2 rational surface. However, there are no direct confirmation in the present observation. Further investigation is necessary.

Chapter 6

Conclusion

The heavy ion beam probe have been applied to measure MHD instability for the first time in a helical system. The development of complete beam control system in the CHS HIBP enable us to carry out this measurement. In this thesis, two major works as diagnostic improvement are described, followed by the physics interpretation of the observed MHD oscillation. The experimental calibrations using a movable detector system and gas ionization method are successfully accomplished. The movable detector was used to determine the sweep voltage set to observe the plasma center, confirming the beam line alignment. Then sets of deflector voltages to observe locations along a radial scan line were experimentally obtained using gas ionization method. The results agree well with the calculation. Calibrations were generally successful, but improvement in the movable detector is necessary for more accurate calibration.

The HIBP has been applied to measure the local space potential and density fluctuations during burst-type MHD activities in a low beta NBI plasma. Various non local effects (path integral effects along the beam trajectories) have been examined. The effects of beam deflection and acceleration (or deceleration) on local potential fluctuation measurements caused by the fluctuating vector potential are evaluated from the HIBP experimental data combined with magnetic probe

signals based on the simple model vector potentials. Taking those effects into account, the radial structures of the m/n = 2/1 burst type MHD oscillation has been clarified.

The potential fluctuation is localized around the q = 2 surface in the growing phase. The mode is propagating in the ion diamagnetic direction with changing the phase relation between magnetic fluctuation and potential fluctuation. The mode is considered to be pressure driven interchange instability. On the other hand, the potential fluctuation is suppress at all over the plasma radii in the decaying phase. The mode appears to be fixed to the E×B fluid rotation. These results seems to be suggesting m=2 island formation at the q=2 rational surface, although more direct confirmation is necessary in future.

The present result demonstrates a new diagnostic approach to MHD fluctuation studies in helical plasmas.

References

[1] J. Wesson: *Tokamaks*. Oxford Science Publications, New York (1987).

[2] JET TEAM: Nucl. Fusion **32**(1992)187.

[3] P. Freidberg: *Ideal magnetohydrodynamics*. Plenum Press, New York and London, (1987).

[4] B. Lehnert: Plasma Phys. **9**(1967)301.

[5] J. H. Harris, et. al: Phys. Rev. Lett. **53**(1984)2242.

[6] M. Wakatani, Y. Nakamura and K. Ichiguchi: Fusion Engineering and Design **15** (1992)395.

[7] S. C. McCool, et. al: J. Nucl. Materials **176**(1990)716

[8] H. Sugama and M. Wakatani: J. Phys. Soc. Jpn. **58**(1989)1128.

[9] K. Itoh, S-I. Itoh and A. Fukuyama: Phys. Rev. Lett. **69**(1992)1050.

[10] Y. Hamada, et. al: *Proc. IAEA Conf. Plasma Physics and Controlled Nuclear Fusion, Seville, 1994, IAEA-CN-60/A2-16.*

[11] Ch. P. Ritz, et. al: Phys. Rev. Lett. **62**(1989)1844.

[12] T.P. Crowley, et. al: Nucl. Fusion **32**(1992)1295.

[13] Y. Hamada, et. al: Nucl. Fusion **36**(1996) 515

[14] J. C. Hosea, et. al: Phys. Rev. Lett. **30**(1973)839.

[15] P. L. Colestock, et. al: Phys. Rev. Lett. **26**(1978)1717.

[16] G. A. Hallock, et. al: Phys. Rev. Lett. **21**(1987)1301.

[17] X. Z. Yang, et. al: Phys. Fluids B **3**(1991)3448.

[18] K.A. Connor, et. al: Rev. Sci. Instrum. **63**(1992)4505.

[19] A. Fujisawa, et. al: Rev. Sci. Instrum. **63** (1992)3694.

[20] R. B. White: *Hand Book of Plasma Physics*. North Holland, Amsterdam(1983).

[21] J. A. Wesson: Plasma Physics. **26** (1984)789.

[22] K. McGuire, et. al: Phys. Rev. Lett. **50**(1983)891.

[22'] R.J.Fonck, et.al: Rev. Sci. Instrum. **61** (1990)3487.

[23] R. L. Hickok and F. C. Jobes: AFOSR Science Report. AFORS TR-72-0018 (1972)

[24] D.R. Hertling, R.K. Feeney, D.W. Hughes and W.E. Sayle II: J. Appl. Phys. **53** (1982)5427.

[25] L. Solensten and K.A. Connor: Rev. Sci. Instrum. **58** (1987)516.

[26] T. S. Green and G. A. Proca: Rev. Sci. Instrum. **41** (1970)1409.

[27] A. Carnevali, J.R. Misium, J.F. Lewis and K.A. Connor: Rev. Sci. Instrum. **57** (1986)1822.

[28] R. K. Feeney, et. al: Rev. Sci. Instrum. **47** (1976)964.

[29] K. Ooi, et. al: Langmuir. **7** (1991)1167.

[30] A. N. Pargellis and M. Seidi: J. Appl. Phys. **49** (1978)4933.

[31] P. Spadtke: Sci. Instrum. **65** (1994)1419.

[32] P. Spadtke, et. al: Sci. Instrum. **65** (1994)1441.

[33] A. Fujisawa, et. al: Rev. Sci. Instrum. **67** (1996)3099.

[34] A. Fujisawa, H. Iguchi and Y. Hamada: Rev. Sci. Instrum. **65**(1994)1580.

[35] T.P. Crowley: IEEE. Nucl. Plasma Sci. Soc. **22**(1994)291.

[36] S. Lee, et. al: to be published in Fusion Engineering and Design.

[37] J. J. Zielinski, et. al: Rev. Sci. Instrum. **63**(1992)4574.

[38] T.P. Crowley, et. al: to be published in Fusion Engineering and Design.

[39] S. Sakakibara, et. al: J. Phys. Soc. Jpn. **63**(1994)4406.

[40] S. Sakakibara, et. al: Jpa. J. Appl. Phy. **34**(1995)**L**252 Part2.

[41] S. Okamura, et. al: Nucl. Fusion **35**(1995)283.

[42] S. Okamura, et. al: *Proc. IAEA Conf. Plasma Physics and Controlled Nuclear Fusion, Seville, 1994, IAEA-CN-60/A2-20.*

[43] K. Ida, H. Yamada, H. Iguchi, S. Hidekuma, H. Sanuki and K. Yamazaki: Phys. Fluids B **3**(1991)515.

[44] H. Idei, et. al: Phys. Plasmas. **1**(1994)3400.

[45] V.J. Simcic, et. al: Rev. Sci. Instrum. **61**(1990)3061.

[46] V.J. Simcic, et. al: Phys. Fluids B **5**(1993)1576.

[47] K. Ichiguchi, et. al: Nucl. Fusion **29**(1989)2093.

[48] S. P. Hirshman: Computer Physics Communications. **43**(1986)143.

[49] A. Fujisawa, et. al: to be published in Rev. Sci. Instrum.

[50] D.W. Ross, et. al: Nucl. Fusion **31**(1991)1355.

[51] D.W. Ross, et. al: Rev. Sci. Instrum. **63**(1992)2232.

[52] J. W. Heard, et. al: Rev. Sci. Instrum. **64**(1993)1001.

[53] J. G. Schwelberger, et. al: Rev. Sci. Instrum. **63**(1992)4571.

[54] J. G. Schwelberger, et. al: IEEE. Nucl. Plasma Sci. Soc. **22**(1994)321.

[55] C. X. Yu, et. al: Phys. Fluids B **4**(1992)381.

[56] D. L. Brower, et. al: Phys. Rev. Lett. **59**(1987)48.

[57] M. Wakatani, et. al: Nucl. Fusion **24**(1984)1407.

[58] B.D. Scott, et. al: Phys. Fluids **28**(1985)275.

[59] K. Toi, et. al: *Proc. IAEA Conf. Plasma Physics and Controlled Nuclear Fusion, Seville, 1994, IAEA-CN-60/A6/C-P3.*